

The search for continuous gravitational waves: metric of the multi-detector \mathcal{F} -statistic

Reinhard Prix

Max-Planck-Institut für Gravitationsphysik, Albert-Einstein-Institut, Am Mühlenberg 1, 14476 Golm, Germany

We develop a general formalism for the parameter-space metric of the multi-detector \mathcal{F} -statistic, which is a matched-filtering detection statistic for continuous gravitational waves. We find that there exists a whole *family* of \mathcal{F} -statistic metrics, parametrized by the (unknown) amplitude parameters of the gravitational wave. The multi-detector metric is shown to be expressible in terms of noise-weighted *averages* of single-detector contributions, which implies that the number of templates required to cover the parameter space does *not* scale with the number of detectors. Contrary to using a longer observation time, combining detectors of similar sensitivity is therefore the computationally cheapest way to improve the sensitivity of coherent wide-parameter searches for continuous gravitational waves.

We explicitly compute the \mathcal{F} -statistic metric family for signals from isolated spinning neutron stars, and we numerically evaluate the quality of different metric approximations in a Monte-Carlo study. The metric predictions are tested against the measured mismatches and we identify regimes in which the local metric is no longer a good description of the parameter-space structure.

I. INTRODUCTION

Continuous gravitational waves (GWs), which would be emitted, for example, by spinning non-axisymmetric neutron stars, or by solar-mass binary systems, are generally expected to be so weak that they will be buried several orders of magnitude below the noise of even the most sensitive detectors. The detection of such signals therefore requires the exact knowledge of their waveform, in order to be able to coherently correlate the data with the expected signal by *matched filtering*.

In a wide-parameter search for unknown sources, however, we typically only know the family of possible waveforms (or an approximation thereof), parametrized by unknown signal parameters (such as the frequency or sky position of the source). The corresponding parameter space needs to be covered by a finite number of “templates” for which a search will be performed. These templates must be placed densely enough, so that for any possible signal, no more than a certain fraction of the signal-to-noise ratio (SNR) is lost at the closest template. On the other hand, coherently correlating the data with every templates is computationally expensive and increases the number of statistical false-alarm candidates. Therefore an *optimal* covering is desirable, which minimizes the number of templates but guarantees the required “minimal match”.

In order to solve this *covering problem*, it is essential to understand the underlying parameter-space structure. Most studies on the construction of optimal template banks have been performed in the context of binary-inspiral searches. It was realized early on that a geometric approach to this problem is the most natural, in particular the introduction of a *metric* on the parameter space by Balasubramanian et al. [1] and Owen [2], building on the earlier concept of the “fitting factor” introduced by Apostolatos [3]. Note, however, that this definition of the metric differs subtly from the “canonical” definition used in the present work (and also in [4]), which is derived directly from the detection statistic (see

appendix A for more details). The canonical definition of the metric assigns the relative loss of SNR due to an offset in signal parameters as an invariant “distance” measure, which can locally be expressed as a metric tensor. The metric is closely related to the well-known concept of the “Fisher information matrix”, which quantifies the statistical errors in the parameter estimation of signals: the (canonical) metric is identical to the *normalized* Fisher matrix, even though it describes conceptually rather different aspects of the detection statistic.

A somewhat related question is the *global* parameter-space structure, which was studied in [5] for the case of isolated neutron-star signals. This study found that the global structure (the “circles in the sky”) deviates significantly from the local metric picture. The global structure is relevant, for example, for deciding whether different detection candidates are consistent with the same signal, i.e. whether they are “coincident candidates”. Obviously, the metric description is the local approximation to this global parameter-space structure.

In this paper we consider gravitational-wave signals that are nearly monochromatic and sinusoidal in the frame of the GW source, and which are of long duration (i.e. typically longer than the observation time T). This class of signals is usually referred to as “continuous waves”, and the prime examples are GWs from non-axisymmetric spinning neutron stars (e.g. see [6] for a review) and stellar-mass binary systems in the LISA frequency band (e.g. see [4]).

The phase of the signal received at the detector is Doppler modulated by the rotation and orbital motion of the detector. The observed phase therefore depends not only on the intrinsic frequency evolution of the signal, but also on its sky position. In addition to the phase modulation, there is a time-varying amplitude modulation, due to the rotating antenna pattern of the detector. This amplitude modulation depends on the polarization angle ψ and the polarization amplitudes A_+ and A_\times of the GW. However, as shown by Jaranowski et al. [7], these unknown parameters (together with the initial

phase ϕ_0), can be eliminated by analytically maximizing the detection statistic. The resulting reduced parameter space includes only the parameters affecting the time evolution of the signal phase, which we will refer to as the ‘‘Doppler parameters’’. This amplitude-maximized detection statistic is generally known as the ‘‘ \mathcal{F} -statistic’’, which has been used in several searches for continuous GWs from spinning neutron stars (e.g. [8, 9, 10]). After two earlier (partly successful) attempts to generalize the \mathcal{F} -statistic to a coherent network of detectors [4, 7], this problem was fully solved more recently by Cutler and Schutz [11].

Somewhat surprisingly, however, there has not been much work on the metric of the \mathcal{F} -statistic, neither in the single- nor the multi-detector case: the single-detector \mathcal{F} -statistic metric was derived on a formal level by Królak et al. [4], but was not evaluated explicitly or studied further. A single-detector \mathcal{F} -statistic metric was used (without giving any details) in [12] to numerically estimate the number of templates in galactic-binary searches with LISA. An earlier study by Brady et al. [13] of the metric for isolated neutron-star signals introduced a metric approximation based only on the phase modulation of the signal and neglecting the amplitude modulation. We will refer to this approximation as the ‘‘phase metric’’. This metric has a simpler structure than the full \mathcal{F} -metric, and it can be computed analytically [14] if one assumes a circular orbital motion. This is the only type of continuous GW metric that is currently implemented in LAL/LALApps [15].

As we will see in this study, the amplitude modulation cannot always be neglected, but ‘‘on average’’ the phase metric seems to be a good approximation, and its quality improves with longer observation times and with the number of detectors. With the recent multi-detector generalization of the \mathcal{F} -statistic formalism [11] and its subsequent implementation into LAL/LALApps, the need to understand the *multi-detector* \mathcal{F} -statistic metric has become more urgent. The most important question in this context is whether the metric resolution increases with the number of detectors, i.e. whether a denser covering of the parameter space is required, which would increase the computational cost.

The main result of this work is to show that the metric resolution does *not* scale with the number of detectors. Therefore, sensitivity can be gained at the cost of only a linear increase in the required computing power (as the signal has to be correlated with the data stream from each detector). This has to be contrasted with the (at least) $\mathcal{O}(T^5)$ scaling (117) of the number of templates with observation time T , in the case isolated neutron-star signals with one spindown.

In order to improve the sensitivity of a coherent search for continuous gravitational waves, increasing the number of similar-sensitivity detectors is therefore computationally much cheaper than to increase the observation time.

The plan of this paper is as follows: in Sect. II we in-

roduce the formalism and notation of the multi-detector \mathcal{F} -statistic, following [11] and [4]. In Sect. III we derive the \mathcal{F} -statistic metric family for high-frequency signals (relevant for ground-based detector networks). We compute the extremal range of this metric family, its average metric, and the long-duration limit, in which the \mathcal{F} -metric family reduces to a simple ‘‘orbital metric’’. In Sect. IV we apply this framework to the special case of GWs from isolated spinning neutron stars, and we evaluate the quality of the metric predictions (and different approximations) by comparing them against measured mismatches in a Monte-Carlo study. The main results are summarized in Sect. V. Appendix A presents an alternative, more elegant derivation of the \mathcal{F} -statistic metric, and Appendix B gives the general expressions for the \mathcal{F} -metric, which would be valid also for low-frequency signals relevant for LISA.

II. THE MULTI-DETECTOR \mathcal{F} -STATISTIC

A. General definitions

In this section we introduce the formalism and notation of the \mathcal{F} -statistic, a matched-filtering detection statistic for continuous gravitational waves, which was first introduced by Jaranowski et al. [7], and subsequently generalized to the multi-detector case by Cutler and Schutz [11]. As shown in [7], the dimensionless strain signal $s^X(t)$ of a continuous gravitational wave at detector X can be represented in the form

$$s^X(t) = \sum_{\mu=1}^4 \mathcal{A}^\mu h_\mu^X(t), \quad (1)$$

in terms of four signal-amplitudes \mathcal{A}^μ , which are independent of the detector X, and the detector-dependent basis waveforms $h_\mu^X(t)$. The four amplitudes \mathcal{A}^μ can be expressed in terms of two polarization amplitudes A_+ , A_\times , the initial phase ϕ_0 in the solar-system barycenter (SSB) at a reference time τ_{ref} , and the polarization angle ψ of the wave frame with respect to the equatorial coordinate system, namely

$$\begin{aligned} \mathcal{A}^1 &= A_+ \cos \phi_0 \cos 2\psi - A_\times \sin \phi_0 \sin 2\psi, \\ \mathcal{A}^2 &= A_+ \cos \phi_0 \sin 2\psi + A_\times \sin \phi_0 \cos 2\psi, \\ \mathcal{A}^3 &= -A_+ \sin \phi_0 \cos 2\psi - A_\times \cos \phi_0 \sin 2\psi, \\ \mathcal{A}^4 &= -A_+ \sin \phi_0 \sin 2\psi + A_\times \cos \phi_0 \cos 2\psi. \end{aligned} \quad (2)$$

We can further relate the two polarization amplitudes A_+ and A_\times to the overall amplitude h_0 and the inclination angle ι of the quadrupole rotation axis with respect to the line of sight, namely

$$A_+ = \frac{1}{2} h_0 (1 + \cos^2 \iota), \quad A_\times = h_0 \cos \iota. \quad (3)$$

The four basis waveforms $h_\mu^X(t)$ can be written as

$$\begin{aligned} h_1^X(t) &= a^X(t) \cos \phi^X(t), & h_2^X(t) &= b^X(t) \cos \phi^X(t), \\ h_3^X(t) &= a^X(t) \sin \phi^X(t), & h_4^X(t) &= b^X(t) \sin \phi^X(t), \end{aligned} \quad (4)$$

where $a^X(t)$ and $b^X(t)$ are the antenna-pattern functions (see Eqs.(12,13) of [7]), and $\phi^X(t)$ is the signal phase at the detector X. The antenna-pattern functions $a^X(t)$, $b^X(t)$ depend on the sky position \vec{n} of the GW source, and on the location and orientation of the detector X. The phase $\phi^X(t)$ also depends on the *intrinsic* phase parameters, ω say, of the signal. In the case of continuous waves from isolated neutron stars, ω would only consist of the $s + 1$ spin parameters, i.e. $\omega = \{f^{(k)}\}_{k=0}^s$, where $f^{(k)}$ is the k -th time-derivative of the intrinsic signal frequency in the SSB (see Sect. IV). In the case of signals from spinning neutron stars in a binary system, ω would also contain the binary orbital parameters. We can summarize these dependencies as

$$a^X = a^X(t; \vec{n}), \quad b^X = b^X(t; \vec{n}), \quad \phi^X = \phi^X(t; \vec{n}, \omega). \quad (5)$$

In the following we denote the set of ‘‘Doppler parameters’’ (i.e. the parameters affecting the time evolution of the phase) by $\lambda \equiv \{\vec{n}, \omega\}$, as opposed to the four ‘‘amplitude parameters’’ $\{\mathcal{A}\}^\mu = \mathcal{A}^\mu$. Note that in the literature the Doppler parameters are sometimes referred to as ‘‘intrinsic’’, and the amplitude parameters as ‘‘extrinsic’’, but we will not use this convention here.

Using the multi-detector notation of [4, 11], we write vectors in ‘‘detector-space’’ in boldface, i.e. $\{\mathbf{s}\}^X = s^X$, and so the signal model (1) can be written as

$$\mathbf{s}(t; \mathcal{A}, \lambda) = \mathcal{A}^\mu \mathbf{h}_\mu(t; \lambda), \quad (6)$$

with implicit summation over repeated amplitude indices, $\mu \in \{1, 2, 3, 4\}$. We assume the data $x^X(t)$ of detector X contains a signal with parameters $\{\mathcal{A}, \lambda\}$ in addition to Gaussian stationary noise $n^X(t)$, i.e.

$$\mathbf{x}(t) = \mathbf{n}(t) + \mathbf{s}(t; \mathcal{A}, \lambda). \quad (7)$$

In general, the noise contributions $n^X(t)$ of the different detectors could be correlated (which might be relevant for the two LIGO detectors in Hanford, or for LISA), and so we define the (double-sided) noise-density matrix S^{XY} as

$$S^{XY}(f) = \int_{-\infty}^{\infty} \kappa^{XY}(\tau) e^{-i2\pi f\tau} d\tau, \quad (8)$$

in terms of the correlation functions

$$\kappa^{XY}(\tau) \equiv E [n^X(t + \tau) n^Y(t)]. \quad (9)$$

The corresponding multi-detector scalar product is defined (in analogy to [16]) as

$$(\mathbf{x}|\mathbf{y}) \equiv \int_{-\infty}^{\infty} \tilde{x}^X(f) S_{XY}^{-1}(f) \tilde{y}^{Y*}(f) df, \quad (10)$$

where $\tilde{x}(f)$ denotes the Fourier-transformed of $x(t)$. We use implicit summation over repeated detector indices, and the inverse noise matrix is defined by $S_{XY}^{-1} S^{YZ} = \delta_X^Z$. In the case of uncorrelated noise, where $S^{XY} = S^X \delta^{XY}$, the scalar product simplifies to

$$(\mathbf{x}|\mathbf{y}) = \sum_X (x^X|y^X), \quad (11)$$

in terms of the usual single-detector scalar product

$$(x^X|y^X) \equiv \int_{-\infty}^{\infty} \frac{\tilde{x}^X(f) \tilde{y}^{X*}(f)}{S^X(f)} df. \quad (12)$$

With the definition (10) of the multi-detector scalar product, the likelihood function for Gaussian stationary noise $\mathbf{n}(t)$ can be written as

$$P(\mathbf{n}(t)|S^{XY}) = k e^{-\frac{1}{2}(\mathbf{n}|\mathbf{n})}, \quad (13)$$

where k is a normalization constant. Using (7) we can express the likelihood of observing data $\mathbf{x}(t)$ in the presence of a signal $\mathbf{s}(t; \mathcal{A}, \lambda)$ as

$$P(\mathbf{x}|\mathcal{A}, \lambda, S^{XY}) = k e^{-\frac{1}{2}(\mathbf{x}|\mathbf{x})} e^{(\mathbf{x}|\mathbf{s}) - \frac{1}{2}(\mathbf{s}|\mathbf{s})}. \quad (14)$$

Using a standard frequentist approach, the optimal detection statistic to decide between the hypothesis of a signal $s = \mathbf{s}(\mathcal{A}, \lambda)$ being present and no signal, $s = 0$, is given by the likelihood ratio $\Lambda(\mathbf{x}; \mathbf{s})$, defined as

$$\ln \Lambda(\mathbf{x}; \mathbf{s}) \equiv \ln \frac{P(\mathbf{x}|\mathbf{s})}{P(\mathbf{x}|0)} = (\mathbf{x}|\mathbf{s}) - \frac{1}{2}(\mathbf{s}|\mathbf{s}). \quad (15)$$

Substituting the signal model (1), the log-likelihood ratio is found as

$$\ln \Lambda(\mathbf{x}; \mathcal{A}, \lambda) = \mathcal{A}^\mu x_\mu - \frac{1}{2} \mathcal{A}^\mu \mathcal{M}_{\mu\nu} \mathcal{A}^\nu, \quad (16)$$

where we defined

$$x_\mu(\lambda) \equiv (\mathbf{x}|\mathbf{h}_\mu), \quad (17)$$

$$\mathcal{M}_{\mu\nu}(\lambda) \equiv (\mathbf{h}_\mu|\mathbf{h}_\nu). \quad (18)$$

We see that the likelihood ratio (16) can be maximized analytically with respect to the unknown amplitudes \mathcal{A}^μ , and the resulting detection statistic for the Doppler parameters λ is the so-called \mathcal{F} -statistic, namely

$$2\mathcal{F}(\mathbf{x}; \lambda) \equiv x_\mu \mathcal{M}^{\mu\nu} x_\nu, \quad (19)$$

where $\mathcal{M}^{\mu\nu} \equiv \{\mathcal{M}^{-1}\}^{\mu\nu}$, i.e. $\mathcal{M}_{\mu\alpha} \mathcal{M}^{\alpha\nu} = \delta_\mu^\nu$. Note that the four (multi-detector) wave-functions $\mathbf{h}_\mu(t)$ form a basis of the signal space, and \mathcal{M} is the associated metric, which allows us to raise and lower amplitude indices. In particular, we could define a ‘‘dual’’ basis, $\mathbf{h}^\mu(t) \equiv \mathcal{M}^{\mu\nu} \mathbf{h}_\nu(t)$, satisfying $(\mathbf{h}^\mu|\mathbf{h}_\nu) = \delta_\nu^\mu$, and the \mathcal{F} -statistic (19) could then be written even more compactly as $2\mathcal{F}(\lambda) = x^\mu x_\mu$.

B. \mathcal{F} -statistic of perfectly matched signals

Let us consider the case where the target Doppler parameters λ are perfectly matched to the signal λ_s , so the measured data would be $\mathbf{x}(t) = \mathbf{n}(t) + \mathbf{s}(t; \mathcal{A}, \lambda)$. In this case, the projections (17) are

$$x_\mu(\mathcal{A}, \lambda) = n_\mu(\lambda) + s_\mu(\mathcal{A}, \lambda), \quad (20)$$

where we defined $n_\mu \equiv (\mathbf{n} | \mathbf{h}_\mu)$ and $s_\mu \equiv (\mathbf{s} | \mathbf{h}_\mu)$. Assuming Gaussian stationary noise, one can show that

$$E[n_\mu] = 0, \quad \text{and} \quad E[n_\mu n_\nu] = \mathcal{M}_{\mu\nu}, \quad (21)$$

where $E[\cdot]$ is the expectation value. We further find

$$E[x_\mu] = s_\mu, \quad \text{and} \quad E[x_\mu x_\nu] = \mathcal{M}_{\mu\nu} + s_\mu s_\nu, \quad (22)$$

so the four random variables x_μ have mean s_μ and covariances $\mathcal{M}_{\mu\nu}$. Using this together with (19), we find the expectation value of the \mathcal{F} -statistic as

$$E[2\mathcal{F}] = 4 + \rho^2(0), \quad (23)$$

in terms of the ‘‘optimal’’ signal-to-noise ratio $\rho(0)$, given by

$$\rho^2(0) = s_\mu \mathcal{M}^{\mu\nu} s_\nu = \mathcal{A}^\mu \mathcal{M}_{\mu\nu} \mathcal{A}^\nu = (\mathbf{s} | \mathbf{s}). \quad (24)$$

Using (22), it is straightforward to show that the quadratic form (19) can be diagonalized as the sum of four squares of Gaussian random variables with unit covariance matrix. This implies that $2\mathcal{F}$ is distributed according to a (non-central) χ^2 -distribution with *four* degrees of freedom, as previously shown by Cutler and Schutz [11]. The corresponding non-centrality parameter of this χ^2 -distribution is $\rho^2(0)$.

C. \mathcal{F} -statistic of mismatched signals

In the case of unknown signal parameters, there will generally be an ‘‘offset’’ $\Delta\lambda$ between the Doppler parameters λ_s of the signal and the target parameters λ , i.e.

$$\lambda = \lambda_s + \Delta\lambda. \quad (25)$$

In this case, the projections (17) can be expressed as

$$x_\mu(\mathcal{A}, \lambda_s; \lambda) = n_\mu(\lambda) + \mathcal{A}^\alpha \mathcal{R}_{\alpha\mu}(\lambda_s; \lambda), \quad (26)$$

where the 4x4 matrix $\mathcal{R}_{\alpha\mu}$ is defined as

$$\mathcal{R}_{\alpha\mu}(\lambda_s; \lambda) \equiv (\mathbf{h}_\alpha(\lambda_s) | \mathbf{h}_\mu(\lambda)). \quad (27)$$

This matrix is generally not symmetric, but evidently satisfies the symmetry relation $\mathcal{R}_{\alpha\mu}(\lambda_s; \lambda) = \mathcal{R}_{\mu\alpha}(\lambda; \lambda_s)$. Using this together with (19), we can write the mismatched (SNR)² as

$$\begin{aligned} \rho^2(\mathcal{A}, \lambda_s; \lambda) &\equiv E[2\mathcal{F}] - 4 \\ &= \mathcal{A}^\alpha \mathcal{R}_{\alpha\mu}(\lambda_s; \lambda) \mathcal{M}^{\mu\nu}(\lambda) \mathcal{R}_{\beta\nu}(\lambda_s; \lambda) \mathcal{A}^\beta. \end{aligned} \quad (28)$$

Assuming the target parameters λ to be ‘‘close’’ (in a suitable sense) to the signal, we can Taylor-expand these matrices around the signal-location λ_s , and keeping only terms up to second order, we obtain

$$\begin{aligned} \mathcal{M}^{\mu\nu}(\lambda) &= \mathcal{M}^{\mu\nu}(\lambda_s) + \partial_i \mathcal{M}^{\mu\nu}(\lambda_s) \Delta\lambda^i \\ &\quad + \frac{1}{2} \partial_{ij} \mathcal{M}^{\mu\nu}(\lambda_s) \Delta\lambda^i \Delta\lambda^j, \end{aligned} \quad (29)$$

$$\begin{aligned} \mathcal{R}_{\mu\nu}(\lambda_s; \lambda) &= \mathcal{M}_{\mu\nu}(\lambda_s) + \mathcal{R}_{\mu\nu i}(\lambda_s) \Delta\lambda^i \\ &\quad + \frac{1}{2} \mathcal{R}_{\mu\nu ij}(\lambda_s) \Delta\lambda^i \Delta\lambda^j, \end{aligned} \quad (30)$$

where indices i, j refer to the Doppler parameters λ^i (with automatic summation), and where we defined

$$\mathcal{R}_{\mu\nu i} \equiv (\mathbf{h}_\mu | \partial_i \mathbf{h}_\nu), \quad (31)$$

$$\mathcal{R}_{\mu\nu ij} \equiv (\mathbf{h}_\mu | \partial_{ij} \mathbf{h}_\nu), \quad (32)$$

with $\partial_i \equiv \partial/\partial\lambda^i$ and $\partial_{ij} \equiv \partial^2/\partial\lambda^i \partial\lambda^j$. Substituting these expansions into (28), we find to second order

$$\rho^2(\Delta\lambda) = \mathcal{A}^\mu [\mathcal{M}_{\mu\nu} + \mathcal{L}_{\mu\nu i} \Delta\lambda^i - \mathcal{G}_{\mu\nu ij} \Delta\lambda^i \Delta\lambda^j] \mathcal{A}^\nu, \quad (33)$$

where the first- and second-order coefficients explicitly read as

$$\mathcal{L}_i \equiv \mathcal{R}_i + {}^T \mathcal{R}_i + \mathcal{M} \cdot \partial_i \mathcal{M}^{-1} \cdot \mathcal{M}, \quad (34)$$

$$\begin{aligned} -\mathcal{G}_{ij} &\equiv \frac{1}{2} (\mathcal{R}_{ij} + {}^T \mathcal{R}_{ij}) + \frac{1}{2} \mathcal{M} \cdot \partial_{ij} \mathcal{M}^{-1} \cdot \mathcal{M} \\ &\quad + \mathcal{M} \cdot \partial_i \mathcal{M}^{-1} \cdot {}^T \mathcal{R}_j + \mathcal{R}_i \cdot \mathcal{M}^{-1} \cdot {}^T \mathcal{R}_j \\ &\quad + \mathcal{R}_i \cdot \partial_j \mathcal{M}^{-1} \cdot \mathcal{M}, \end{aligned} \quad (35)$$

using matrix notation, and writing T for the transpose of the *amplitude indices*. By applying derivatives to the identity $\mathcal{M} \cdot \mathcal{M}^{-1} = \mathbb{I}$, we find

$$\mathcal{M} \cdot \partial_i \mathcal{M}^{-1} \cdot \mathcal{M} = -\partial_i \mathcal{M}, \quad (36)$$

$$\mathcal{M} \cdot \partial_{ij} \mathcal{M}^{-1} \cdot \mathcal{M} = -\partial_{ij} \mathcal{M} + 2\partial_i \mathcal{M} \cdot \mathcal{M}^{-1} \cdot \partial_j \mathcal{M}, \quad (37)$$

and using (18) and the product rule, we further obtain

$$\partial_i \mathcal{M} = \mathcal{R}_i + {}^T \mathcal{R}_i, \quad (38)$$

$$\partial_{ij} \mathcal{M} = \mathcal{R}_{ij} + {}^T \mathcal{R}_{ij} + 2h_{ij}, \quad (39)$$

where we defined

$$h_{\mu\nu ij} \equiv (\partial_i \mathbf{h}_\mu | \partial_j \mathbf{h}_\nu). \quad (40)$$

For simplicity of notation, we assume the Doppler indices in (35) to be implicitly symmetrized, i.e. $\mathcal{G}_{ij} = \mathcal{G}_{ji}$, as any non-symmetric parts will not contribute to the quadratic form (33). Using the identities (36)–(39), we can reduce the expansion coefficients (34), (35) to

$$\mathcal{L}_i = 0, \quad (41)$$

$$\mathcal{G}_{ij} = h_{ij} - {}^T \mathcal{R}_i \cdot \mathcal{M}^{-1} \cdot \mathcal{R}_j. \quad (42)$$

The exact vanishing of the first-order coefficient \mathcal{L}_i shows that the perfectly-matched case, $\lambda = \lambda_s$, is a local extremum of the \mathcal{F} -statistic, as expected. The zeroth-order

term in (33) corresponds to the perfectly-matched case (24), and so we arrive at

$$\rho^2(\Delta\lambda) = \rho^2(0) - \mathcal{A}^\mu \mathcal{G}_{\mu\nu ij} \mathcal{A}^\nu \Delta\lambda^i \Delta\lambda^j + \mathcal{O}(\Delta\lambda^3), \quad (43)$$

where $G_{\mu\nu ij}$ can be written more explicitly as

$$\mathcal{G}_{\mu\nu ij} = (\partial_i \mathbf{h}_\mu | \partial_j \mathbf{h}_\nu) - (\mathbf{h}_\alpha | \partial_i \mathbf{h}_\mu) \mathcal{M}^{\alpha\beta} (\mathbf{h}_\beta | \partial_j \mathbf{h}_\nu). \quad (44)$$

As discussed in [4], this matrix is directly related to the *projected Fisher matrix* $\bar{\Gamma}$, namely

$$\bar{\Gamma}_{ij} \equiv \mathcal{A} \cdot \mathcal{G}_{ij} \cdot \mathcal{A}, \quad (45)$$

describing the statistical information on the Doppler parameters λ^i , given the amplitude parameters \mathcal{A}^μ .

III. THE \mathcal{F} -STATISTIC METRIC FAMILY

A. General definitions

The relative loss in expected \mathcal{F} -statistic due to an offset $\Delta\lambda$ with respect to the signal location λ_s defines a natural dimensionless “mismatch”¹ $m_{\mathcal{F}}$, namely

$$m_{\mathcal{F}}(\mathcal{A}, \lambda_s; \Delta\lambda) \equiv \frac{\rho^2(0) - \rho^2(\Delta\lambda)}{\rho^2(0)}. \quad (46)$$

Using (43) for the mismatched SNR, we can cast the \mathcal{F} -mismatch in the form

$$m_{\mathcal{F}} = g_{ij}^{\mathcal{F}}(\mathcal{A}, \lambda) \Delta\lambda^i \Delta\lambda^j + \mathcal{O}(\Delta\lambda^3), \quad (47)$$

where we defined the \mathcal{F} -statistic metric $g_{ij}^{\mathcal{F}}$ as

$$g_{ij}^{\mathcal{F}}(\mathcal{A}, \lambda) \equiv \frac{\mathcal{A} \cdot \mathcal{G}_{ij}(\lambda) \cdot \mathcal{A}}{\mathcal{A} \cdot \mathcal{M}(\lambda) \cdot \mathcal{A}} = \frac{\bar{\Gamma}_{ij}}{\rho^2(0)}. \quad (48)$$

This expression is identical to that found previously (for the single-detector case) in [4, 17], referred to as the “normalized projected Fisher matrix”. A more elegant method of obtaining this result by projecting the full parameter-space metric into the Doppler subspace is shown in appendix A. It is obvious from (46) that the overall signal amplitude h_0 cancels out, and that the mismatch $m_{\mathcal{F}}$ is therefore, contrary to the Fisher matrix $\bar{\Gamma}_{ij}$, independent of h_0 .

The Fisher matrix $\bar{\Gamma}_{ij}$ characterizes the *statistical* uncertainty (due to the presence of noise) of the maximum-likelihood estimators for the signal parameters. In particular, the inverse Fisher matrix gives lower bounds on the variances of the parameter estimators (the so-called Cramér-Rao bound), describing the typical fluctuations by which the location of the detection-statistic peak will

vary in *repeated* experiments. The Fisher matrix can therefore be regarded as a measure of the best possible *accuracy* of parameter estimation. The concept of the metric $g_{ij}^{\mathcal{F}}$, on the other hand, describes the relative (i.e. SNR-independent) “extent” of detection-statistic peaks for any *single* realization of the noise. This gives a measure of the intrinsic parameter-space *resolution*, which is not related to the true location of any putative signal. However, while conceptually rather different, Eq. (48) shows that there exists a deep connection between the two concepts.

The \mathcal{F} -metric (48) is not a unique metric on the Doppler-parameter space λ of the \mathcal{F} -statistic, as it depends on the (generally unknown) signal amplitudes \mathcal{A}^μ . Expression (48) therefore describes a whole family of metrics, corresponding to different $\mathcal{A} = \text{const.}$ subspaces of the full parameter space, which is of very limited direct use for the covering problem of the Doppler-parameter space.

However, we can explicitly compute the possible *range* of mismatches for any given λ and $\Delta\lambda$. For this, consider the extrema of $m_{\mathcal{F}}$ as a function of \mathcal{A} , i.e.

$$0 = \frac{\partial m_{\mathcal{F}}}{\partial \mathcal{A}} = \frac{2\mathcal{G}\mathcal{A}}{\mathcal{A}\mathcal{M}\mathcal{A}} - \frac{\mathcal{A}\mathcal{G}\mathcal{A}}{(\mathcal{A}\mathcal{M}\mathcal{A})^2} 2\mathcal{M}\mathcal{A}, \quad (49)$$

where we wrote $\mathcal{G} \equiv \mathcal{G}_{ij} \Delta\lambda^i \Delta\lambda^j$, which is a 4x4 matrix in amplitude space. Equation (49) is equivalent to

$$(\mathcal{M}^{-1} \cdot \mathcal{G}) \mathcal{A} = \hat{m}_{\mathcal{F}}(\lambda, \Delta\lambda) \mathcal{A}, \quad (50)$$

which determines the extremal values $\hat{m}_{\mathcal{F}}$ of the \mathcal{F} -mismatch as the *eigenvalues* of $\mathcal{M}^{-1} \cdot \mathcal{G}$. According to the Rayleigh principle, the minimum and maximum of the mismatch will be given respectively by the smallest and largest eigenvalues. As suggested in [17], a more practical mismatch measure can be constructed from the *mean* of the eigenvalues, and we can define an “average” \mathcal{F} -metric as

$$\bar{g}_{ij}^{\mathcal{F}}(\lambda) \equiv \frac{1}{4} \text{Tr} [\mathcal{M}^{-1} \cdot \mathcal{G}_{ij}], \quad (51)$$

where the trace Tr refers to the amplitude indices. This average \mathcal{F} -metric, contrary to $g_{ij}^{\mathcal{F}}$, is *independent* of the amplitudes \mathcal{A}^μ , and is therefore of more practical interest as a metric on the Doppler-parameter space. The corresponding average \mathcal{F} -mismatch $\bar{m}_{\mathcal{F}}$ is simply

$$\bar{m}_{\mathcal{F}}(\lambda, \Delta\lambda) \equiv \bar{g}_{ij}^{\mathcal{F}}(\lambda) \Delta\lambda^i \Delta\lambda^j. \quad (52)$$

We note that in the analogous case of binary-inspiral signals, where one can equally maximize the detection statistic over some of the signal parameters (referred to as “extrinsic” parameters), the metric of the reduced parameter space depends again on both extrinsic and intrinsic parameters [18, 19]. A common choice of mismatch metric for the template placement in this binary-inspiral context is to use the most conservative case (based on the

¹ See appendix A for a discussion of a slightly different mismatch definition sometimes found in the literature.

concept of the ‘‘minimal match’’ [2]), namely the worst-case mismatch

$$\widehat{m}_{\mathcal{F}}^{\max}(\lambda, \Delta\lambda) = \max_{\mathcal{A}} m_{\mathcal{F}}(\mathcal{A}, \lambda; \Delta\lambda). \quad (53)$$

This is referred to as the ‘‘minimax’’ prescription in [18]. Contrary to the average metric (52), this extremal metric cannot be expressed as a quadratic form in the Doppler separations $\Delta\lambda$, and so the corresponding iso-mismatch surfaces are not described by hyper-ellipsoids.

As we will see in the following section, for the type of narrow-band continuous-wave signals considered here, the 4x4 matrix $\mathcal{M}^{-1} \cdot \mathcal{G}$ has only *two* independent eigenvalues, corresponding directly to the maximum and minimum possible \mathcal{F} -mismatches for any given λ and $\Delta\lambda$.

B. Narrow-band signals, uncorrelated noise

In the following we restrict our analysis to continuous gravitational waves with a well-defined, slowly varying (intrinsic) frequency f . This assumption applies, for example, for GWs emitted from spinning non-axisymmetric neutron stars, and from stellar-mass binary systems (relevant for LISA). We assume the observation time T to be much longer than the GW period $1/f_s$, such that the number of cycles N is large, i.e.

$$N = f_s T \gg 1. \quad (54)$$

The phase $\phi(t)$ of the signal will be dominated by the zeroth-order term $2\pi f_s t$, while the intrinsic frequency variability and the Doppler modulations are much smaller corrections. Assuming two such narrow-band signals $x(t)$ and $y(t)$, we can approximate the scalar product (10) as

$$\langle \mathbf{x} | \mathbf{y} \rangle \approx T S_{XY}^{-1}(f_s) \langle x^X y^Y \rangle, \quad (55)$$

in terms of the time-averaging operator $\langle \cdot \rangle$, defined as

$$\langle g \rangle \equiv \frac{1}{T} \int_0^T g(t) dt. \quad (56)$$

Note that the noise matrix $S^{XY}(f_s)$ can be considered as a metric in ‘‘detector space’’, allowing us to lower and raise detector indices, e.g. we could write $x_X(t) \equiv S_{XY}^{-1}(f_s) x^Y(t)$, and the scalar product (55) would then read as $\langle \mathbf{x} | \mathbf{y} \rangle = T \langle x^X y_X \rangle$.

For simplicity, we restrict our analysis to the (more common) case of uncorrelated detector noises, i.e. we assume $S_{XY}^{-1} = S_X^{-1} \delta_{XY}$, which allows us to introduce ‘‘noise weights’’ w_X as

$$w_X \equiv \frac{S_X^{-1}}{S^{-1}}, \quad \text{with} \quad S^{-1} \equiv \sum_X S_X^{-1}, \quad (57)$$

such that $\sum w_X = 1$. Using this, the scalar product (55) can now be expressed as

$$\langle \mathbf{x} | \mathbf{y} \rangle = T S^{-1} \langle x y \rangle_S, \quad (58)$$

where we introduced the *noise-weighted averaging* operator $\langle \cdot \rangle_S$, defined as

$$\langle Q \rangle_S \equiv \sum_X w_X \langle Q^X \rangle. \quad (59)$$

The scalar products involved in the expression for the \mathcal{F} -statistic consist of products of slowly varying antenna-pattern functions $g(t) \in \{a(t), b(t)\}$, and highly oscillatory, quasi-periodic functions $p(t) \in \{\sin^2 \phi(t), \cos^2 \phi(t), \sin \phi(t) \cos \phi(t)\}$. In the following we approximate the oscillatory functions as exactly periodic with period $\tau = 1/f$, i.e. $\phi \approx 2\pi f t$, and so we can write the time-average $\langle g p \rangle$ as

$$\langle g p \rangle = \frac{1}{T} \sum_{n=0}^{N-1} \int_{t_n}^{t_{n+1}} g(t) p(t) dt, \quad (60)$$

where $t_n \equiv n\tau$, and $N = T/\tau$ is the number of oscillation cycles. We can Taylor-expand $g(t)$ in each of the periods as $g(t) = g(t_n) + \dot{g}(t_n)(t - t_n) + \frac{1}{2}\ddot{g}(t_n)(t - t_n)^2 + \dots$, and using the fact that

$$\frac{1}{\tau} \int_{t_n}^{t_{n+1}} (t - t_n)^m p(t) dt = \langle t^m p \rangle_{\tau}, \quad (61)$$

where $\langle \cdot \rangle_{\tau}$ denotes the time-average over one cycle of $p(t)$, we obtain the expansion

$$\begin{aligned} \langle g p \rangle &\approx \frac{\langle p \rangle_{\tau}}{T} \sum g(t_n) \tau + \frac{\langle t p \rangle_{\tau}}{T} \sum \dot{g}(t_n) \tau + \dots \\ &\approx \langle p \rangle_{\tau} \langle g \rangle + \frac{\langle t p \rangle_{\tau}}{T} [g(T) - g(0)] + \dots \end{aligned} \quad (62)$$

For the averages over one cycle τ we find:

$$\begin{aligned} \langle \sin^2 \phi \rangle_{\tau} &= \langle \cos^2 \phi \rangle_{\tau} = \frac{1}{2}, \quad \langle \sin \phi \cos \phi \rangle_{\tau} = 0, \\ \langle t^m \sin^2 \phi \rangle_{\tau} &\sim \langle t^m \cos^2 \phi \rangle_{\tau} \sim \langle t^m \sin \phi \cos \phi \rangle_{\tau} \sim \tau^m. \end{aligned} \quad (63)$$

Under the above assumptions, we can therefore write

$$\langle g p \rangle \approx \langle g \rangle \langle p \rangle + \mathcal{O}(1/N), \quad (64)$$

and so we can neglect higher-order contributions and keep only the zeroth-order term $\langle p \rangle \langle g \rangle$ in expressions of this type. Using this approximation, the 4x4 matrix $\mathcal{M}_{\mu\nu}$, defined in (18), is explicitly found as

$$\mathcal{M}_{\mu\nu} \approx \frac{1}{2} S^{-1} T \begin{pmatrix} \mathcal{C} & 0 \\ 0 & \mathcal{C} \end{pmatrix}, \quad (65)$$

where \mathcal{C} is the 2x2 matrix

$$\mathcal{C} \equiv \begin{pmatrix} A & C \\ C & B \end{pmatrix}, \quad (66)$$

in terms of the three independent antenna-pattern coefficients

$$A \equiv \langle a^2 \rangle_S, \quad B \equiv \langle b^2 \rangle_S, \quad C \equiv \langle a b \rangle_S, \quad (67)$$

and we further define $D \equiv AB - C^2$. Inserting the explicit expressions (2) for the amplitudes \mathcal{A}^μ and using (65), we can write the optimal SNR (24) explicitly as

$$\rho^2(0) = \frac{1}{2} h_0^2 T \mathcal{S}^{-1} [\alpha_1 A + \alpha_2 B + 2\alpha_3 C], \quad (68)$$

in terms of the amplitudes (writing $\eta \equiv \cos \iota$):

$$\begin{aligned} \alpha_1(\eta, \psi) &\equiv \frac{1}{4}(1 + \eta^2)^2 \cos^2 2\psi + \eta^2 \sin^2 2\psi, \\ \alpha_2(\eta, \psi) &\equiv \frac{1}{4}(1 + \eta^2)^2 \sin^2 2\psi + \eta^2 \cos^2 2\psi, \\ \alpha_3(\eta, \psi) &\equiv \frac{1}{4}(1 - \eta^2)^2 \sin 2\psi \cos 2\psi. \end{aligned} \quad (69)$$

We see that the optimal SNR does not depend on the initial phase ϕ_0 , and it scales linearly with the overall amplitude h_0 , and with the square-root of the observation time T . The dependence on the number of detectors will be discussed in the next section.

C. Dependence on the number of detectors \mathcal{N}

A question of central importance is how the SNR and the metric resolution depend on the number \mathcal{N} of coherently combined detectors. The dependence of the optimal SNR is very easy to see: in the explicit expression (68), the antenna-pattern coefficients A, B, C are the noise-weighted averages (67) over detector-specific quantities, and the only *scaling* with the number of detectors \mathcal{N} therefore comes from the total inverse noise floor $\mathcal{S}^{-1} = \sum_X \mathcal{S}_X^{-1}$. If we assume, for simplicity, that all \mathcal{N} detectors have a similar noise floor S_0 , i.e. $\mathcal{S}^{-1} \approx \mathcal{N} S_0^{-1}$, then the optimal SNR scales as

$$\rho(0) \propto \frac{h_0}{\sqrt{S_0}} \sqrt{T \mathcal{N}}. \quad (70)$$

Doubling the number of detectors (of similar noise floor) therefore has the same effect on the SNR as doubling the observation time T .

It is not difficult to see from (58) and definitions (18) and (44), that both the numerator and denominator in (48) have the same scaling with \mathcal{S}^{-1} (and therefore \mathcal{N}), which cancels out. To show this more clearly, we write the explicit expression found from Eq. (48) for the multi-detector \mathcal{F} -metric, namely

$$g_{ij}^{\mathcal{F}} = \frac{\mathcal{A}^\mu \left[\langle \partial_i h_\mu \partial_j h_\nu \rangle_S - \langle h_\alpha \partial_i h_\nu \rangle_S \langle h_\alpha h_\beta \rangle_S^{-1} \langle h_\beta \partial_j h_\nu \rangle_S \right] \mathcal{A}^\nu}{\mathcal{A}^\rho \langle h_\rho h_\sigma \rangle_S \mathcal{A}^\sigma}.$$

It is evident from this expression that the \mathcal{F} -metric only depends on noise-weighted averages of single-detector contributions, but does not scale with \mathcal{N} . Note, however, that the multi-detector metric is *not* a simple average of single-detector metrics.

Increasing the number of detectors therefore does not increase the metric resolution in parameter space. This is in strong contrast to the effect of increasing the observation time T , in which case the metric resolution, and

therefore the number of templates, grows at a high power of T (e.g. $\propto \mathcal{O}(T^5)$, see (117)). We can therefore gain $\text{SNR} \propto \sqrt{\mathcal{N}}$ with \mathcal{N} similar-sensitivity detectors, at the cost of “only” a linear increase $\propto \mathcal{N}$ in the required computing power. Using a coherent multi-detector search is therefore the computationally cheapest way to increase SNR in a coherent wide-parameter search for continuous gravitational waves.

As discussed in Sect. III A, the metric *resolution* must not be confused with the *accuracy* of parameter-estimation. The latter increases with SNR (and therefore also with the number of detectors), as described by the Fisher information matrix, while the former does not. It might still seem somewhat surprising that the additional “information” coming from the time delays between detectors does not result in a higher metric sky resolution. This can be understood in terms of the diffraction limit, which can be used to estimate the order of magnitude of the sky resolution from the ratio of the wavelength c/f to the “baseline” VT , where V is the orbital velocity. The expected metric sky resolution is therefore of the order $\Delta\Omega_0 \sim c/(TfV)$, which is exactly the metric scaling found in Sect. IV B. It is therefore evident that for detector distances of the order $\sim 1,000$ km, the “integration baseline” VT dominates the sky resolution starting from observation times as short as $T \gtrsim 100$ s, and no additional sky resolution can be gained from the baseline spanned by different detectors.

D. The \mathcal{F} -metric family for high-frequency signals

In order to explicitly calculate the \mathcal{F} -metric family (71), we need to consider the derivatives $\partial_i h_\mu^X$ of the basis functions (4), namely (omitting detector indices)

$$\begin{aligned} \partial_i h_1 &= \partial_i a \cos \phi - a \partial_i \phi \sin \phi, \\ \partial_i h_2 &= \partial_i b \cos \phi - b \partial_i \phi \sin \phi, \\ \partial_i h_3 &= \partial_i a \sin \phi + a \partial_i \phi \cos \phi, \\ \partial_i h_4 &= \partial_i b \sin \phi + b \partial_i \phi \cos \phi. \end{aligned} \quad (71)$$

The antenna-pattern functions $a(t), b(t)$ do not depend on any of the Doppler parameters λ except for the sky position \vec{n} . From their explicit expressions (cf. Eqs.(12,13) of [7]) for *ground-based* interferometers one sees that

$$\partial_{\vec{n}} a \sim a \sim \mathcal{O}(1), \quad \partial_{\vec{n}} b \sim b \sim \mathcal{O}(1), \quad (72)$$

while the corresponding phase derivatives will typically be of order

$$|\partial_{\vec{n}} \phi(t)| \sim \left| \partial_t \phi \frac{\vec{r}(t)}{c} \right| \sim 2\pi f \frac{r_{\text{orb}}}{c} + 2\pi f T V / c + \dots \quad (73)$$

Ignoring the constant term, which will not contribute to the metric, the second term will be much larger than unity if the number of cycles $N = fT$ satisfies $N \gg c/V \sim 10^4$. This will always be true for high-frequency signals relevant for ground-based detectors, for which we

can therefore neglect the antenna-pattern derivatives in (71) with respect to the phase derivatives, i.e.

$$\partial_i \phi \gg \partial_i a, \partial_i b, \quad (74)$$

This assumption might not hold in the case of low-frequency signals that would be more relevant for LISA, or for very short observation times. The corresponding calculations are somewhat more tedious, but lead to equivalent results and are presented in appendix B. Using (74), (58) and keeping only the leading-order terms in (64), we can approximate (40) as

$$h_{\mu\nu ij} \approx \frac{1}{2} \mathcal{S}^{-1} T \begin{pmatrix} P_{ij}^1 & P_{ij}^3 & 0 & 0 \\ P_{ij}^3 & P_{ij}^2 & 0 & 0 \\ 0 & 0 & P_{ij}^1 & P_{ij}^3 \\ 0 & 0 & P_{ij}^3 & P_{ij}^2 \end{pmatrix}, \quad (75)$$

with the three independent components

$$\begin{aligned} P_{ij}^1 &= \langle a^2 \partial_i \phi \partial_j \phi \rangle_S, & P_{ij}^2 &= \langle b^2 \partial_i \phi \partial_j \phi \rangle_S, \\ P_{ij}^3 &= \langle a b \partial_i \phi \partial_j \phi \rangle_S. \end{aligned} \quad (76)$$

In the same way, (31) can be approximated as

$$\mathcal{R}_{\mu\nu i} \approx \frac{1}{2} \mathcal{S}^{-1} T \begin{pmatrix} 0 & 0 & R_i^{13} & R_i^{14} \\ 0 & 0 & R_i^{14} & R_i^{24} \\ -R_i^{13} & -R_i^{14} & 0 & 0 \\ -R_i^{14} & -R_i^{24} & 0 & 0 \end{pmatrix}, \quad (77)$$

where

$$\begin{aligned} R_i^{13} &= \langle a^2 \partial_i \phi \rangle_S, & R_i^{24} &= \langle b^2 \partial_i \phi \rangle_S, \\ R_i^{14} &= \langle a b \partial_i \phi \rangle_S. \end{aligned} \quad (78)$$

Using this and (65), we obtain

$$\{\text{Tr} \mathcal{R}_i \mathcal{M}^{-1} \mathcal{R}_j\}_{\mu\nu} \approx \frac{1}{2} \mathcal{S}^{-1} T \begin{pmatrix} Q_{ij}^1 & Q_{ij}^3 & 0 & 0 \\ Q_{ij}^3 & Q_{ij}^2 & 0 & 0 \\ 0 & 0 & Q_{ij}^1 & Q_{ij}^3 \\ 0 & 0 & Q_{ij}^3 & Q_{ij}^2 \end{pmatrix}, \quad (79)$$

with the three independent components

$$\begin{aligned} D Q_{ij}^1 &= A \langle a b \partial_i \phi \rangle_S \langle a b \partial_j \phi \rangle_S + B \langle a^2 \partial_i \phi \rangle_S \langle a^2 \partial_j \phi \rangle_S \\ &\quad - 2C \langle a^2 \partial_i \phi \rangle_S \langle a b \partial_j \phi \rangle_S, \end{aligned} \quad (80)$$

$$\begin{aligned} D Q_{ij}^2 &= A \langle b^2 \partial_i \phi \rangle_S \langle b^2 \partial_j \phi \rangle_S + B \langle a b \partial_i \phi \rangle_S \langle a b \partial_j \phi \rangle_S \\ &\quad - 2C \langle a b \partial_i \phi \rangle_S \langle b^2 \partial_j \phi \rangle_S, \end{aligned} \quad (81)$$

$$\begin{aligned} D Q_{ij}^3 &= A \langle a b \partial_i \phi \rangle_S \langle b^2 \partial_j \phi \rangle_S + B \langle a b \partial_i \phi \rangle_S \langle a^2 \partial_j \phi \rangle_S \\ &\quad - C [\langle b^2 \partial_i \phi \rangle_S \langle a^2 \partial_j \phi \rangle_S + \langle a b \partial_i \phi \rangle_S \langle a b \partial_j \phi \rangle_S], \end{aligned} \quad (82)$$

assuming implicit index symmetrization in i, j . Combining this with (75) and (44), we find the 4x4 amplitude matrix $\mathcal{G}_{\mu\nu}$ in the form

$$\mathcal{G}_{\mu\nu} \approx \frac{1}{2} \mathcal{S}^{-1} T \begin{pmatrix} m^1 & m^3 & 0 & 0 \\ m^3 & m^2 & 0 & 0 \\ 0 & 0 & m^1 & m^3 \\ 0 & 0 & m^3 & m^2 \end{pmatrix}, \quad (83)$$

in terms of the three independent mismatch components

$$m^r(\lambda; \Delta\lambda) = m_{ij}^r \Delta\lambda^i \Delta\lambda^j, \quad (84)$$

where $r \in \{1, 2, 3\}$, and the corresponding matrices are

$$m_{ij}^r(\lambda) \equiv P_{ij}^r - Q_{ij}^r. \quad (85)$$

In analogy to (68), we can write the projected Fisher matrix (45) as

$$\bar{\Gamma}_{ij} = \frac{1}{2} h_0^2 T \mathcal{S}^{-1} [\alpha_1 m_{ij}^1 + \alpha_2 m_{ij}^2 + 2\alpha_3 m_{ij}^3], \quad (86)$$

in terms of the amplitudes $\alpha_r = \alpha_r(\cos \iota, \psi)$ defined in (69). This allows us to express the \mathcal{F} -metric family (48) in the more explicit form

$$g_{ij}^{\mathcal{F}}(\cos \iota, \psi; \lambda) \equiv \frac{\alpha_1 m_{ij}^1 + \alpha_2 m_{ij}^2 + 2\alpha_3 m_{ij}^3}{\alpha_1 A + \alpha_2 B + 2\alpha_3 C}. \quad (87)$$

As discussed in Sect. III A, the extrema $\hat{m}_{\mathcal{F}}$ of the mismatch family $m_{\mathcal{F}}(\mathcal{A})$ are given by the eigenvalues of $\mathcal{M}^{-1} \cdot \mathcal{G}$, namely

$$\begin{aligned} 0 &= \det [\mathcal{M}^{-1} \cdot \mathcal{G} - \hat{m}_{\mathcal{F}} \mathbb{I}] \\ &= \det \mathcal{M}^{-1} \det [\mathcal{G} - \hat{m}_{\mathcal{F}} \mathcal{M}], \end{aligned} \quad (88)$$

and therefore

$$0 = (m^1 - \hat{m}_{\mathcal{F}} A)(m^2 - \hat{m}_{\mathcal{F}} B) - (m^3 - \hat{m}_{\mathcal{F}} C)^2. \quad (89)$$

We see that there are maximally *two* independent eigenvalues, namely

$$\hat{m}_{\mathcal{F}}^{\max|\min}(\lambda; \Delta\lambda) = \bar{m}_{\mathcal{F}} \pm \sqrt{\bar{m}_{\mathcal{F}}^2 - \tilde{m}^2}, \quad (90)$$

where

$$\bar{m}_{\mathcal{F}} \equiv (2D)^{-1} [B m^1 + A m^2 - 2C m^3], \quad (91)$$

$$\tilde{m}^2 \equiv D^{-1} [m^1 m^2 - (m^3)^2]. \quad (92)$$

Note that $\tilde{m}^2 > 0$ is necessary for the positivity of the \mathcal{F} -mismatch $m_{\mathcal{F}}$, and is equivalent to the matrix \mathcal{G}_{ij} being positive definite, as can be seen from (83). The extremal solutions (90) determine the maximum and minimum possible mismatch, respectively, as well as the average \mathcal{F} -mismatch $\bar{m}_{\mathcal{F}}$, for given signal location λ and offset $\Delta\lambda$. The corresponding average \mathcal{F} -metric is found from (52) and (91) as

$$\bar{g}_{ij}^{\mathcal{F}}(\lambda) = (2D)^{-1} [B m_{ij}^1 + A m_{ij}^2 - 2C m_{ij}^3]. \quad (93)$$

Note that, contrary to the average mismatch $\bar{m}_{\mathcal{F}}$, the extremal values $\hat{m}_{\mathcal{F}}^{\min|\max}$ cannot be written as quadratic forms in the Doppler offsets $\Delta\lambda$. The range of possible \mathcal{F} -mismatches for given λ and $\Delta\lambda$ can be characterized by an intrinsic ‘‘uncertainty’’ $\Delta m_{\mathcal{F}}$, which we define as

$$\Delta m_{\mathcal{F}}(\lambda; \Delta\lambda) \equiv \frac{1}{2} (\hat{m}_{\mathcal{F}}^{\max} - \hat{m}_{\mathcal{F}}^{\min}) = \sqrt{\bar{m}_{\mathcal{F}}^2 - \tilde{m}^2}, \quad (94)$$

and we further introduce the relative uncertainty $\sigma_{\mathcal{F}}$ as

$$\sigma_{\mathcal{F}}(\lambda; \Delta\lambda) \equiv \frac{\Delta m_{\mathcal{F}}}{\overline{m}_{\mathcal{F}}} = \left(1 - \frac{\tilde{m}^2}{\overline{m}_{\mathcal{F}}^2}\right)^{1/2}, \quad (95)$$

which is bounded in $\sigma_{\mathcal{F}} \in [0, 1]$. The maximal mismatch $\hat{m}_{\mathcal{F}}^{\max}$ can never be larger than *twice* the average mismatch $\overline{m}_{\mathcal{F}}$, and in most cases it will be smaller. The average \mathcal{F} -metric $\overline{g}_{ij}^{\mathcal{F}}$ might therefore be quite a reliable mismatch measure in practice, which will be confirmed in the Monte-Carlo studies in Sect. IV for isolated neutron star signals.

E. Long-duration limit: the ‘‘orbital metric’’

Consider the limit of very long observation times compared to a day τ_d , i.e. $T \gg \tau_d$. We can always write the signal phase $\phi^X(t)$ at the detector X as

$$\phi^X(t) = \phi_{\text{orb}}(t) + \Delta\phi^X(t), \quad (96)$$

where $\phi_{\text{orb}}(t)$ is the signal phase modulated by the orbital motion, while $\Delta\phi^X(t)$ accounts for the additional diurnal phase modulation due to the spin of the earth, which is of order

$$\Delta\phi^X(t) \sim 2\pi f \Delta\tau^X(t), \quad (97)$$

where the time delay $|\Delta\tau^X(t)| \lesssim 0.02$ s is periodic over a day. We restrict ourselves to signals with slowly varying frequency over the timescale of a day (e.g. excluding neutron stars in close binary systems), for which we can assume $\phi_{\text{orb}}(t) \sim 2\pi ft$. With these assumptions and (64), we can approximate the typical contributions to the \mathcal{F} -metric in the following way:

$$\begin{aligned} \langle a^2 \partial_i \phi \rangle_S &= \sum_X w_X \langle a^X a^X \partial_i \phi^X \rangle \\ &= \sum w_X \langle a^X a^X \partial_i \phi_{\text{orb}} \rangle + \sum w_X \langle a^X a^X \partial_i \Delta\phi^X \rangle \\ &\approx \langle \partial_i \phi_{\text{orb}} \rangle \sum w_X \langle a^X a^X \rangle + \langle a^2 \partial_i \Delta\phi \rangle_S. \end{aligned} \quad (98)$$

According to our assumptions, the average $\langle \partial_i \phi_{\text{orb}} \rangle$ is at least linear in the observation time T , while the second term will be roughly constant on timescales longer than a day. In the limit $T \gg \tau_d$ we therefore find

$$\langle a^2 \partial_i \phi \rangle_S \stackrel{T \gg \tau_d}{\approx} A \langle \partial_i \phi_{\text{orb}} \rangle. \quad (99)$$

In the same way, we can approximate in this limit

$$\begin{aligned} P_{ij}^1 &\approx A \phi_{ij}^{\text{orb}}, & P_{ij}^2 &\approx B \phi_{ij}^{\text{orb}}, & P_{ij}^3 &\approx C \phi_{ij}^{\text{orb}}, \\ Q_{ij}^1 &\approx A \phi_i^{\text{orb}} \phi_j^{\text{orb}}, & Q_{ij}^2 &\approx B \phi_i^{\text{orb}} \phi_j^{\text{orb}}, \\ Q_{ij}^3 &\approx C \phi_i^{\text{orb}} \phi_j^{\text{orb}}, \end{aligned} \quad (100)$$

where we defined

$$\phi_i^{\text{orb}} \equiv \langle \partial_i \phi_{\text{orb}} \rangle, \quad \text{and} \quad \phi_{ij}^{\text{orb}} \equiv \langle \partial_i \phi_{\text{orb}} \partial_j \phi_{\text{orb}} \rangle. \quad (101)$$

Introducing the ‘‘orbital metric’’ g_{ij}^{orb} as

$$g_{ij}^{\text{orb}} \equiv \phi_{ij}^{\text{orb}} - \phi_i^{\text{orb}} \phi_j^{\text{orb}}, \quad (102)$$

and the corresponding orbital mismatch m_{orb} ,

$$m_{\text{orb}} \equiv g_{ij}^{\text{orb}} \Delta\lambda^i \Delta\lambda^j, \quad (103)$$

we find the limiting $T \gg \tau_d$ approximations

$$m^1 \approx A m_{\text{orb}}, \quad m^2 \approx B m_{\text{orb}}, \quad m^3 \approx C m_{\text{orb}}. \quad (104)$$

The \mathcal{F} -mismatch range (90) therefore reduces to a single eigenvalue, namely

$$\hat{m}_{\mathcal{F}}^{\min|\max} \stackrel{T \gg \tau_d}{\approx} m_{\text{orb}}, \quad (105)$$

and the multi-detector \mathcal{F} -metric family reduces to the orbital metric (102), i.e.

$$g_{ij}^{\mathcal{F}}(\mathcal{A}, \lambda) \stackrel{T \gg \tau_d}{\approx} g_{ij}^{\text{orb}}(\lambda), \quad (106)$$

which is independent of the unknown amplitudes and of the number and position of detectors.

Note that a different, but related metric approximation is the ‘‘phase metric’’, which neglects the amplitude modulation $a^X(t)$, $b^X(t)$, but retains the detector-specific phase modulation $\Delta\phi^X(t)$, namely

$$g_{ij}^{\phi, X}(\lambda) \equiv \langle \partial_i \phi^X \partial_j \phi^X \rangle - \langle \partial_i \phi^X \rangle \langle \partial_j \phi^X \rangle. \quad (107)$$

While this is intrinsically a single-detector metric, one could formally generalize it by analogy with the \mathcal{F} -metric, and simply replace the time averages $\langle \cdot \rangle$ by noise-weighted multi-detector averages $\langle \cdot \rangle_S$. In this manner we could define an *ad-hoc* multi-detector phase metric as

$$g_{ij}^{\phi}(\lambda) \equiv \langle \partial_i \phi \partial_j \phi \rangle_S - \langle \partial_i \phi \rangle_S \langle \partial_j \phi \rangle_S. \quad (108)$$

IV. APPLICATION TO SIGNALS FROM ISOLATED NEUTRON STARS

In the following we apply the general framework of the previous sections to a particular class of gravitational-wave signals, namely GWs emitted from isolated spinning neutron stars. Restricting ourselves to a specific signal model allows us to explicitly compute the metric and evaluate different approximations for various cases of interest. It also allows us to compare the metric predictions to measured mismatches using a realistic search code for computing the \mathcal{F} -statistic.

A. The phase model

GWs emitted from isolated spinning neutron stars can be described by a very simple phase model, namely

$$\phi^X(t) = 2\pi \sum_{k=0}^s \frac{f^{(k)}(\tau_{\text{ref}})}{(k+1)!} [\tau^X(t)]^{k+1}, \quad (109)$$

where $f^{(k)}$ is the k -th time derivative of the intrinsic signal frequency $f(\tau)$ in the solar-system barycenter (SSB), and $\tau^X(t)$ is the arrival time in the SSB (with respect to the reference time τ_{ref}) of a wavefront reaching the detector X at time t . Neglecting relativistic effects, this relation is simply given by

$$\tau^X(t) = t + \frac{\vec{r}^X(t) \cdot \vec{n}}{c} - \tau_{\text{ref}}, \quad (110)$$

where $\vec{r}^X(t)$ is the position of detector X with respect to the SSB. This can be separated into an orbital and a spin component, namely

$$\vec{r}^X(t) = \vec{r}_{\text{orb}}(t) + \vec{r}_{\text{spin}}^X(t), \quad (111)$$

where \vec{r}_{orb} is the position of the earth in the SSB, and \vec{r}_{spin}^X is the position of the detector on earth. The unit vector \vec{n} denotes the sky position of the source, which can be written as

$$\vec{n} = (\cos \delta \cos \alpha, \cos \delta \sin \alpha, \sin \delta), \quad (112)$$

in terms of the equatorial coordinates *right ascension* α and *declination* δ . For this phase model we have the derivatives

$$\frac{\partial \phi^X(t)}{\partial f^{(k)}} = 2\pi \frac{[\tau^X(t)]^{k+1}}{(k+1)!}, \quad (113)$$

$$\frac{\partial \phi^X(t)}{\partial \vec{n}} = 2\pi \frac{\vec{r}^X(t)}{c} \sum_{k=0}^s \frac{f^{(k)}}{k!} [\tau^X(t)]^k. \quad (114)$$

The intrinsic signal frequency $f(\tau)$ can usually be assumed to be a slowly varying function of time, and typically one only needs to include a small number of spindown coefficients $f^{(k)}$, between $s = 0$ and $s = 3$, say. With these phase derivatives and the explicit antenna-pattern functions $a(t)$, $b(t)$ (Eqs.(12),(13) in [7]), we can numerically compute the different metrics derived in Sect. III.

The corresponding time integrals involved in these expressions were computed numerically using a Gauss-Legendre quadrature of order 2000. This results in a (saturated) convergence of the metric components g_{ij} and the antenna-pattern integrals A, B, C at the level of a relative precision of 10^{-10} , while the corresponding mismatches, $m = g_{ij} \Delta \lambda^i \Delta \lambda^j$, only converge to a level of about 10^{-5} . The weaker convergence of m is can be attributed to the fact that the metrics are highly ill-conditioned matrices, as will be discussed further in Sect. IV E 2.

B. Natural units for the Doppler offsets $\Delta \lambda$

We can easily find the scaling and the order of magnitudes of the metric components: keeping only the dominant scaling-terms in the phase derivatives (113), (114) we find

$$\partial_{f^{(k)}} \phi^X \sim t^{k+1}, \quad \partial_{\vec{n}} \phi^X \sim f \vec{r}_{\text{orb}}(t)/c. \quad (115)$$

Taylor-expanding $\vec{r}_{\text{orb}}(t)$ for “short” observation times $T \ll 1$ year, and neglecting the antenna-pattern functions $a(t) \sim b(t) \sim \mathcal{O}(1)$, we find the following scaling for the metric components (107):

$$\begin{aligned} g_{f^k f^{k'}} &\sim T^{k+1} T^{k'+1}, \\ g_{n^i n^j} &\sim (fV/c)^2 T^2 e_i e_j, \\ g_{f^k n^i} &\sim T^{k+1} fTV/c e_i, \end{aligned} \quad (116)$$

where e^i is the unit vector along the orbital velocity V^i . These estimates allow us to read off the (minimal) scaling of the metric determinant $g = \det g_{ij}$ and of the corresponding volume measure \sqrt{g} , namely

$$\sqrt{g} \sim f^2 \mathcal{O}(T^2) \prod_{k=0}^s T^{k+1}, \quad (117)$$

where s is the number of spindown coefficients to include. Note that the dominant term (116) of the sky metric $g_{n^i n^j}$ is degenerate and will only be regularized by higher order terms. Therefore the scaling of the number of sky templates will be *at least* of the order $\mathcal{O}(T^2)$, but is likely to be higher. If we consider the case of a single spindown, i.e. $s = 1$, we find the scaling for the volume (and therefore number of templates) of the order $\sqrt{g} \sim f^2 \mathcal{O}(T^5)$.

In order for these metric components to be dimensionless and of order unity, we should measure the Doppler offsets $\Delta \lambda^i$ in terms of “natural units” $\Delta \lambda_0^i$, namely

$$\Delta f_0^{(k)} \equiv 1/T^{k+1}, \quad \Delta n_0 \equiv c/(fTV), \quad (118)$$

where $V/c \approx 10^{-4}$. We denote the Doppler offsets in natural units as

$$\widehat{\Delta \lambda}^i \equiv \Delta \lambda^i / \Delta \lambda_0^i. \quad (119)$$

Note that \vec{n} is the unit vector pointing to a sky location, and using its expression (112) in terms of equatorial coordinates α, δ , we find

$$|\Delta \vec{n}|^2 = \cos^2 \delta (\Delta \alpha)^2 + (\Delta \delta)^2. \quad (120)$$

For small offsets, $|\Delta \vec{n}|$ is simply the angular distance corresponding to offsets $\Delta \alpha$ and $\Delta \delta$. We therefore define the natural-unit angular offset $\Delta \widehat{\Omega}$ on the sky as

$$\Delta \widehat{\Omega} \equiv \frac{|\Delta \vec{n}|}{\Delta n_0}. \quad (121)$$

In these units, the statement of “small” Doppler offsets in the expansion (43) is really meaningful, i.e. the validity of the metric approximation is guaranteed in the regime

$$\Delta \widehat{f}^{(k)} \ll 1, \quad \Delta \widehat{\Omega} \ll 1. \quad (122)$$

However, as will be seen later, this condition is in many cases not necessary for the approximate validity of the metric. Note that the metric iso-mismatch ellipses on

the sky are highly anisotropic (the dominant contribution shown in (116) is in fact degenerate), and the actual metric scale can therefore deviate significantly from $\Delta\hat{\Omega}$, depending on the direction of the angular offset. In fact, $\Delta\hat{\Omega}$ corresponds to the larger of the two angular eigenvalues on the sky (resulting in the smaller mismatch-scale), but it nevertheless captures the correct scaling of the sky metric.

C. Numerical exploration of the parameter space

The results in the following sections are based on Monte-Carlo simulations of the parameter space of signals and Doppler offsets. Here we summarize how the underlying random distributions are generated. For the signal amplitudes \mathcal{A}^μ , given in (2), we pick $\cos \iota$ and ψ with uniform distributions from the ranges $\cos \iota \in [-1, 1]$ and $\psi \in [0, \pi]$. We simply fix the overall amplitude to $h_0 = 1$ and the initial phase to $\phi_0 = 0$, as these parameters have no effect on the metric. The Doppler parameters λ^i of the signal are picked (with uniform distributions) from the ranges $f \in [100, 200]$ Hz, $\dot{f} \in [-10^{-9}, 10^{-9}] s^{-2}$, $\alpha \in [0, 2\pi]$ and $\sin \delta \in [-1, 1]$. Note that δ is picked in such a way as to obtain an *isotropic* distribution of points $\{\alpha, \delta\}$ on the sky sphere.

The appropriate selection of random Doppler offsets $\Delta\lambda^i$ is more delicate, because their distribution should be roughly “isotropic” in some metric sense, and the corresponding \mathcal{F} -mismatches should lie in a “reasonable” range, where the metric approximation is applicable, e.g. $m_{\mathcal{F}} \leq 0.5$ say. Note that the second requirement is irrelevant for the purpose of studying intrinsic properties of the metric and for comparing different metric approximations with each other. However, it is essential for a comparison of the metric predictions to *measured* \mathcal{F} -mismatches, which will be described in Sect. IV G.

We use the following algorithm to generate suitable Doppler offsets $\Delta\lambda^i$, satisfying the above requirements:

1. Pick the signal parameters \mathcal{A}^μ and λ^i as described above, and compute the corresponding \mathcal{F} -metric $g_{ij}^{\mathcal{F}}(\cos \iota, \psi; \lambda)$ at this parameter-space point.
2. Pick a random offset vector $\Delta\hat{\lambda}^i$ in natural units with a uniform distribution in the hypercube, i.e. $\Delta\hat{\lambda}^i \in [-1, 1]$. The corresponding dimensional offsets $\Delta\lambda^i$ are therefore uniformly distributed in $\Delta f' \in [-\Delta f_0, \Delta f_0]$, $\{\Delta\alpha', \Delta\delta'\} \in [-\Delta n_0, \Delta n_0]$, and $\Delta\dot{f}' \in [-\Delta\dot{f}_0, \Delta\dot{f}_0]$
3. Normalize $\Delta\lambda^i$ using the metric, i.e. construct $e_{\Delta}^i \equiv \Delta\lambda^i / |\Delta\lambda'|$, where $|\Delta\lambda'| = \sqrt{g_{ij}^{\mathcal{F}} \Delta\lambda^i \Delta\lambda^j}$
4. Pick a distance $d \equiv \sqrt{m}$ with uniform distribution in $d \in [0.1, \sqrt{0.5}]$.
5. The resulting Doppler offset is then obtained as $\Delta\lambda^i = d e_{\Delta}^i$.

The lower bound of $m_{\mathcal{F}} \geq 0.01$ on the generated \mathcal{F} -mismatches is chosen in order to avoid numerical errors dominating the relative differences between mismatches, which happens especially when comparing to measured mismatches. We typically generate about 250,000 random choices of signal parameters and offsets, for observation times ranging from $T = 12$ hours to $T = 200$ hours in steps of 4 hours, which corresponds to about 5000 trials for each choice of observation time. By construction, the distribution of $m_{\mathcal{F}}$ is such that $\sqrt{m_{\mathcal{F}}}$ is uniformly distributed in the range $[0.1, \sqrt{0.5}]$. The distribution of the Doppler offsets $\Delta\hat{\lambda}$ in natural units is found to be approximately Gaussian with zero mean and a standard deviation of about 0.3. There are, however, a few percent of offsets reaching up to a few hundreds in natural units, which corresponds to highly degenerate directions of the metric.

D. Intrinsic uncertainty of the \mathcal{F} -metric

As discussed in Sect. II A, the reduced parameter space of the \mathcal{F} -statistic is the Doppler space λ , while the amplitude space \mathcal{A} has been “projected out” by maximization. For the problem of covering the Doppler-parameter space with templates, the amplitudes represent *unknown* external parameters, and so we cannot directly use the \mathcal{F} -metric family $g_{ij}^{\mathcal{F}}(\mathcal{A}, \lambda)$ for the covering problem. However, as shown in Sect. III B, we can compute an average \mathcal{F} -metric $\bar{g}_{ij}^{\mathcal{F}}(\lambda)$, and a corresponding intrinsic relative uncertainty $\sigma_{\mathcal{F}}(\lambda, \Delta\lambda)$, which are both independent of the unknown amplitudes \mathcal{A} . This uncertainty range in

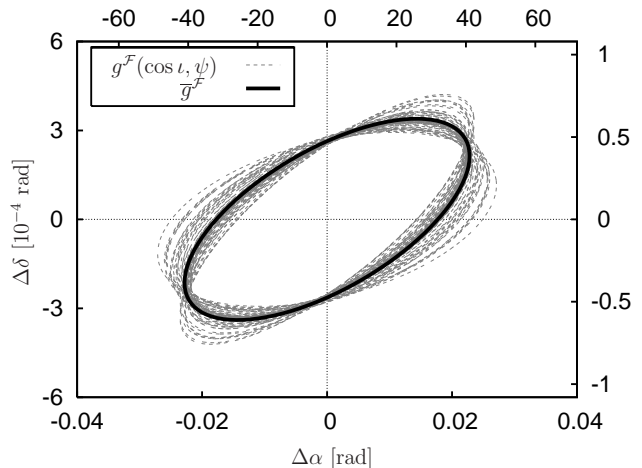


FIG. 1: Iso-mismatch ($m = 0.1$) ellipses of the \mathcal{F} -metric family $g_{ij}^{\mathcal{F}}(\cos \iota, \psi; \lambda)$ for 100 random choices $\{\cos \iota, \psi\}$, and of the average metric $\bar{g}_{ij}^{\mathcal{F}}(\lambda)$. Parameter-space cut along the sky plane $\{\alpha, \delta\}$. The top and right-hand axes show the corresponding offsets in natural units. [Parameters: $f = 100$ Hz, $\alpha = 1.45$ rad, $\delta = 0$ rad, $\dot{f} = 0$, detector = ‘L1’, GPS start-time $t_0 = 810720013$ s, duration $T = 50$ hours.]

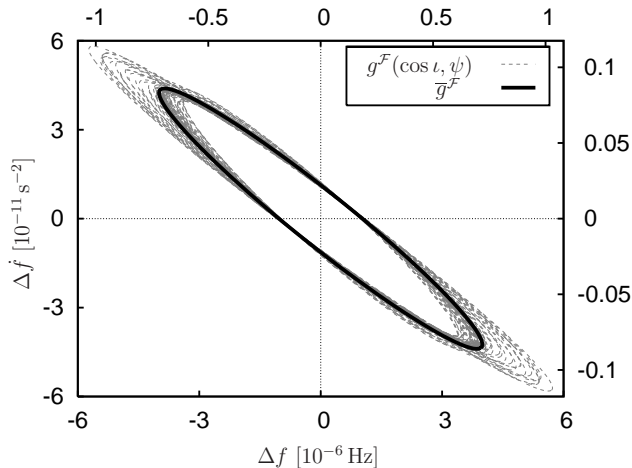


FIG. 2: Same as Fig. 1 for a parameter-space cut along the $\{f, \dot{f}\}$ plane. The top and right-hand axes show the corresponding offsets in natural units.

the predicted mismatch is illustrated in Fig. 1 and Fig. 2, which show different parameter-space cuts through the iso-mismatch hyper-ellipsoids for the average metric $\bar{g}_{ij}^{\mathcal{F}}$ and for 100 randomly picked members of the \mathcal{F} -metric family $g^{\mathcal{F}}(\cos \iota, \psi)$. Note that the *intersection* of all these mismatch hyper-ellipsoids $m_{\mathcal{F}} < 0.1$ corresponds to the worst-case mismatch region $\hat{m}_{\mathcal{F}}^{\max} < 0.1$, which is clearly not a hyper-ellipsoid. Fig. 3 shows the distribution of the

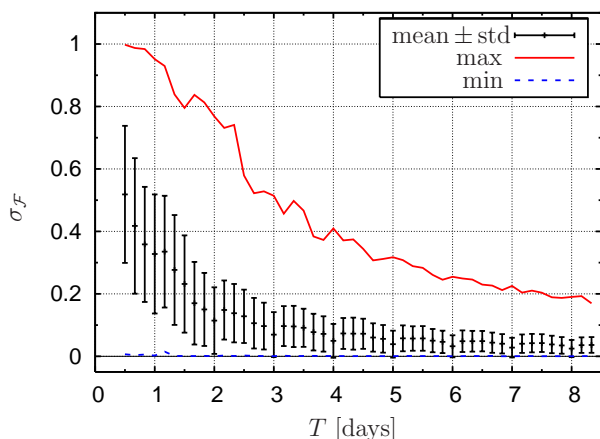


FIG. 3: Distribution of the relative intrinsic uncertainty $\sigma_{\mathcal{F}}$ of the \mathcal{F} -mismatch as a function of observation time T , for the single-detector case. Plotted are the mean, standard deviation and extremal values of the distribution for each value of T .

relative uncertainty $\sigma_{\mathcal{F}}(\lambda, \Delta\lambda)$, as a function of the observation time T for randomly chosen signal parameters and offsets (using the algorithm described in Sect. IV C). These results are for the single-detector case only, the corresponding dependence on the number of detectors is investigated in Sect. IV F. We see in Fig. 3 that for short

observation times, of the order of $T \sim 12$ hours, the relative uncertainty can be as large as 100%. For longer observation times of the order of a few days, $\sigma_{\mathcal{F}}$ decreases substantially, but even for $T \sim 8$ days, the intrinsic uncertainty can still reach up to about 20 %.

E. Comparing different metric approximations

For the following comparisons of different metric approximations, it will be useful to define the *relative error* $\varepsilon(a, b)$ between two quantities a and b as

$$\varepsilon(a, b) \equiv \frac{a - b}{(|a| + |b|)/2}, \quad (123)$$

which is the harmonic mean of $(a - b)/|a|$ and $(a - b)/|b|$. This definition has the advantage of being bound within $[-2, 2]$ even for large deviations $a \gg b$ or $b \gg a$, while it agrees with the more common definitions of relative errors for small values $|\varepsilon| \ll 1$.

1. Monte-Carlo study of mismatches

As we have seen in Fig. 3, the intrinsic relative uncertainty $\sigma_{\mathcal{F}}$ decreases substantially on the timescale of a few days, corresponding to a convergence $g_{ij}^{\mathcal{F}} \rightarrow \bar{g}_{ij}^{\mathcal{F}}$. The average metric $\bar{g}_{ij}^{\mathcal{F}}$ is therefore expected to be an increasingly reliable approximation of the full \mathcal{F} -metric $g_{ij}^{\mathcal{F}}$ with longer observation times T . This is indeed the case, as

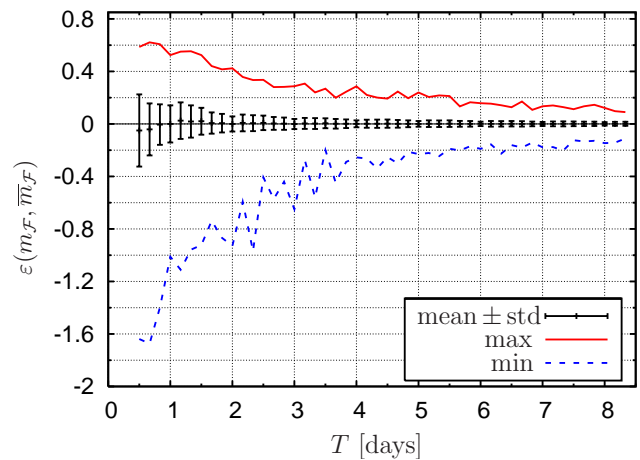


FIG. 4: Distribution of relative errors $\varepsilon(m_{\mathcal{F}}, \bar{m}_{\mathcal{F}})$ of the (single-detector) average \mathcal{F} -mismatch $\bar{m}_{\mathcal{F}}$ with respect to the exact \mathcal{F} -mismatch $m_{\mathcal{F}}$ as a function of observation time T . Plotted are the mean, standard deviation and extremal values of the distribution for each value of T .

can be seen in Fig. 4, which shows the distribution of relative errors $\varepsilon(m_{\mathcal{F}}, \bar{m}_{\mathcal{F}})$ as a function of observation time T . This distribution was obtained using random choices of the signal parameters and Doppler offsets as described

in Sect. IV C. The standard deviation of the relative errors is about 20 % for short observation times $T \lesssim 1$ day, but rapidly decreases to about 1 % for timescales of a few days. Note that these errors are somewhat smaller than could have been expected from the intrinsic uncertainty $\sigma_{\mathcal{F}}$ shown in Fig. 3, which indicates that mismatches near the extremal values $m_{\mathcal{F}}^{\min|\max}$ are less likely than those closer to the average $\bar{m}_{\mathcal{F}}$.

As shown in Sect. III E, the \mathcal{F} -metric family $g_{ij}^{\mathcal{F}}$ converges to the orbital metric g_{ij}^{orb} for very long observation times $T \gg 1$ day, but it is not obvious on which timescales this convergence happens in practice. Fig. 5

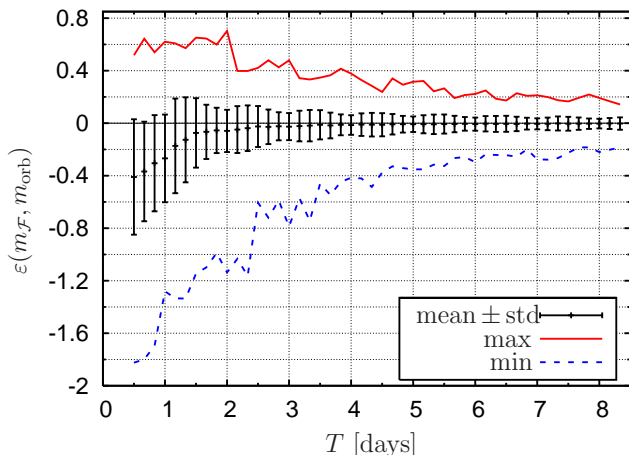


FIG. 5: Distribution of relative errors $\varepsilon(m_{\mathcal{F}}, m_{\text{orb}})$ of the orbital metric with respect to the (single-detector) \mathcal{F} -metric as a function of observation time T . Plotted are the mean, standard deviation and extremal values of the distribution for each value of T .

shows the relative errors $\varepsilon(m_{\mathcal{F}}, m_{\text{orb}})$ of the orbital metric compared to the exact \mathcal{F} -metric, as a function of observation time. Note that a plot with the distribution of $\varepsilon(m_{\mathcal{F}}, m_{\phi})$ would look virtually indistinguishable. These two metric approximations perform nearly identically as far as predicting mismatches is concerned, as can be seen in Fig. 6 showing the distribution of relative errors $\varepsilon(m_{\phi}, m_{\text{orb}})$. Note that the orbital as well as the phase metric show a tendency to *overestimate* the mismatch for short observation times $T \lesssim 1$ days, which is apparent in Fig. 5. Summarizing, we conclude that the “mismatch quality” of the orbital and of the phase metric seem virtually identical, and both approximations perform only slightly worse than the average \mathcal{F} -metric shown in Fig. 4. However, as will become clear in the next section, there is an important difference between the phase metric and the orbital metric, which does not manifest itself in this Monte-Carlo study due to the smallness of the relevant parameter space in which the difference becomes apparent.

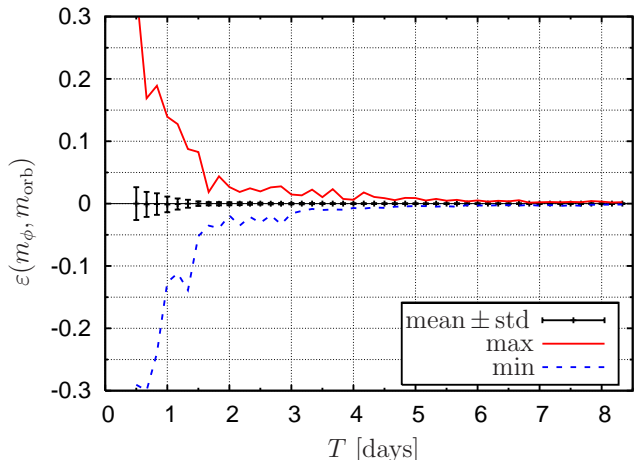


FIG. 6: Distribution of relative errors $\varepsilon(m_{\phi}, m_{\text{orb}})$ of the orbital metric with respect to the phase metric as a function of observation time T . Plotted are the mean, standard deviation and extremal values of the distribution for each value of T .

2. Metric determinants and eigenvalues

A complementary way of comparing different metrics is to look at their eigenvalues and determinants. These invariant quantities characterize the semi-major axes and the volume of iso-mismatch hyperellipsoids, which are important properties for the template covering of the parameter space. We denote the four metric eigenvalues as $g_1 \geq g_2 \geq g_3 \geq g_4$. The metric for isolated neutron-star signals is quite generally represented by highly ill-conditioned matrices in the default parameter-space coordinates $(\alpha, \delta, f, \dot{f}, \dots)$. That means that g_1 is typically many orders of magnitude larger than g_4 , corresponding to very thin and elongated mismatch hyperellipsoids. This property can be characterized by the so-called *condition number*, defined as $\kappa \equiv g_1/g_4$. Well-conditioned matrices have $\kappa \sim \mathcal{O}(1)$, while the metrics encountered here typically have $\kappa(g_{ij}^{\mathcal{F}}) \sim 10^{20}$ in SI units, and $\kappa(g_{ij}^{\mathcal{F}}) \sim 10^8$ in natural units (cf. Sect. IV B). Ill-conditioned matrices can strongly amplify numerical errors in computing their maps, inverses, determinants or eigenvalues. One has to be very careful when handling such matrices numerically, as the results can be quite unreliable. Using SI units, it turns out to be all but impossible to compute the determinant or the eigenvalues using standard double-precision arithmetic, which suffers from complete loss of significant digits in this case. In natural units, however, these quantities can be computed (albeit not with good precision, and not for all points in parameter space), and the results for one example are shown in Fig. 7 and Fig. 8. Contrary to the apparent fast convergence of the orbital- and the \mathcal{F} -mismatches shown in Fig. 5, we see a very different picture for the metric determinants in Fig. 7. For timescales of a few days, the determinant of the orbital metric is a few orders of magnitude smaller than the determinants of the other met-

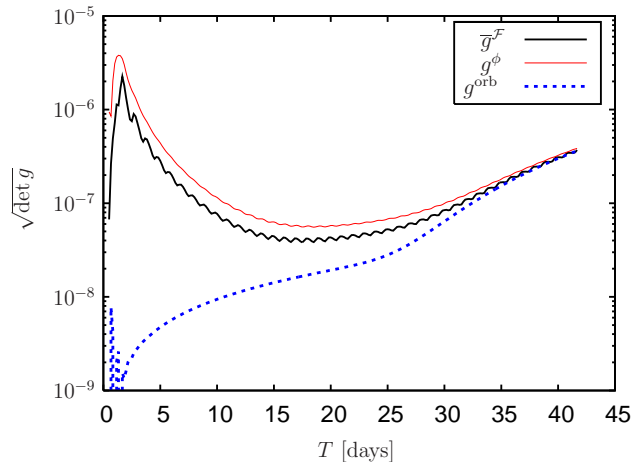


FIG. 7: Determinants of different metric approximations (in natural units) as functions of observation time T . [Parameters: $f = 100$ Hz, $\dot{f} = 0$, $\alpha = 1.0$ rad, $\delta = 0.5$ rad, detector = ‘H1’, GPS start-time $t_0 = 792576013$ s]

ric approximations, and the expected convergence (106) takes place only for timescales longer than $T \gtrsim 1$ month.

How can this be reconciled with the apparently much faster convergence of the mismatches in Fig. 5? In order to better understand this, let us look at the four eigenvalues g_i as functions of T , which is shown in Fig. 8. We see that the largest discrepancy of the orbital metric occurs for the smallest eigenvalue, g_4 , corresponding to the most degenerate direction of the metric. The largest two eigenvalues g_1, g_2 agree well, and g_3 only differs by a factor of a few. In order for the mismatch to be affected by the smallest eigenvalue, we would have to pick a Doppler offset that is *very* closely aligned with the most degenerate principal axis, as any appreciable offset along the other axes would easily dominate the total mismatch. A very rough order-of-magnitude estimate of the probability p of picking such a direction yields an upper bound of $p \lesssim \sqrt{(g_4/g_1)(g_4/g_2)(g_4/g_3)} \lesssim 10^{-6}$. It is therefore very unlikely to pick a Doppler offset for which the mismatch is dominated by the smallest eigenvalue. This is consistent with the fact that in about $\sim 10^5$ trials we did not see any cases in which the orbital metric had dramatically underestimated the mismatch, i.e. where $\varepsilon(m_{\mathcal{F}}, m_{\text{orb}}) \sim 2$ in Fig. 5.

It is interesting to note that while the phase metric seems virtually identical to the orbital metric for “almost all” directions in parameter space, its determinant (and eigenvalues) agree much better with the (average) \mathcal{F} -metric. The small effect of the spin motion of the earth is negligible for most directions in parameter space, except for the most degenerate one, where it substantially reduces the degeneracy.

F. The multi-detector \mathcal{F} -metric

As discussed in Sect. III C, the parameter-space *resolution* of the multi-detector \mathcal{F} -metric does not scale with the number of detectors. Instead, the effect of combining detectors coherently results in a noise-weighted average of contributions from different detectors. This averaging operation (59) would be expected to decrease the effects of the antenna-pattern functions $a^X(t)$ and $b^X(t)$, as well as the detector-specific Doppler modulation $\Delta\phi^X(t)$ of the signal phase (96). In Fig. 9 we see indeed that both the intrinsic uncertainty $\sigma_{\mathcal{F}}$ of the \mathcal{F} -metric family, as well as its relative difference to the orbital metric decrease with the number of detectors. These results are based on a Monte-Carlo simulation with $\sim 40,000$ randomly chosen parameters (see Sect. IV C), for a fixed observation time of $T = 55$ hours, and using between one and six coherently combined detectors. For the sake of this example, we have made the (obviously unrealistic) assumption that all 6 detectors have the same noise floor, otherwise the convergence would be much weaker. Note that we would find exactly the same mismatch convergence for the phase metric as that shown in Fig. 9(b) for the orbital metric.

G. Comparing metric predictions to measured mismatches

In order to validate the theoretical \mathcal{F} -statistic mismatch $m_{\mathcal{F}}$, derived in Sect. III B, we compare it to the measured relative SNR loss m_0 in a simulated mismatched search. This is done by first generating (using `lalapps_Makefakedata` [15]) a fake signal with parameters $\{\mathcal{A}, \lambda_s\}$ picked at random (see Sect. IV C). We then measure (using `lalapps_ComputeFStatistic` [15]) the perfectly-matched SNR $\rho(0)$ at the signal location λ_s , and the mismatched SNR $\rho(\Delta\lambda)$ at an offset Doppler position $\lambda_s + \Delta\lambda$. The offsets $\Delta\lambda$ were picked at random using the algorithm described in Sect. IV C. The *measured* \mathcal{F} -mismatch m_0 is then given simply by the definition Eq. (46). The comparison of the measured mismatches m_0 to the theoretical approximation reveals a problem with the metric approximation for large angular offsets (in natural units), in particular for $\Delta\hat{\Omega} \gtrsim 5$. The origin of this “metric failure” can be understood in terms of the metric curvature and will be discussed in more detail in IV G 2. In the meantime we simply remove this known source of errors by excluding points with $\Delta\hat{\Omega} > 5$, which affects less than 1% of the Monte-Carlo trials. Fig. 10 shows the measured mismatches m_0 as a function of the prediction $m_{\mathcal{F}}$, for observation times of (a) $T = 12$ hours and (b) $T = 60$ hours. We see that there is a substantial scattering of measured mismatches in the case of $T = 12$ hours, which has virtually disappeared for $T = 60$ hours. This second type of “metric failure”, which only affects short observation times, will be discussed in IV G 1.

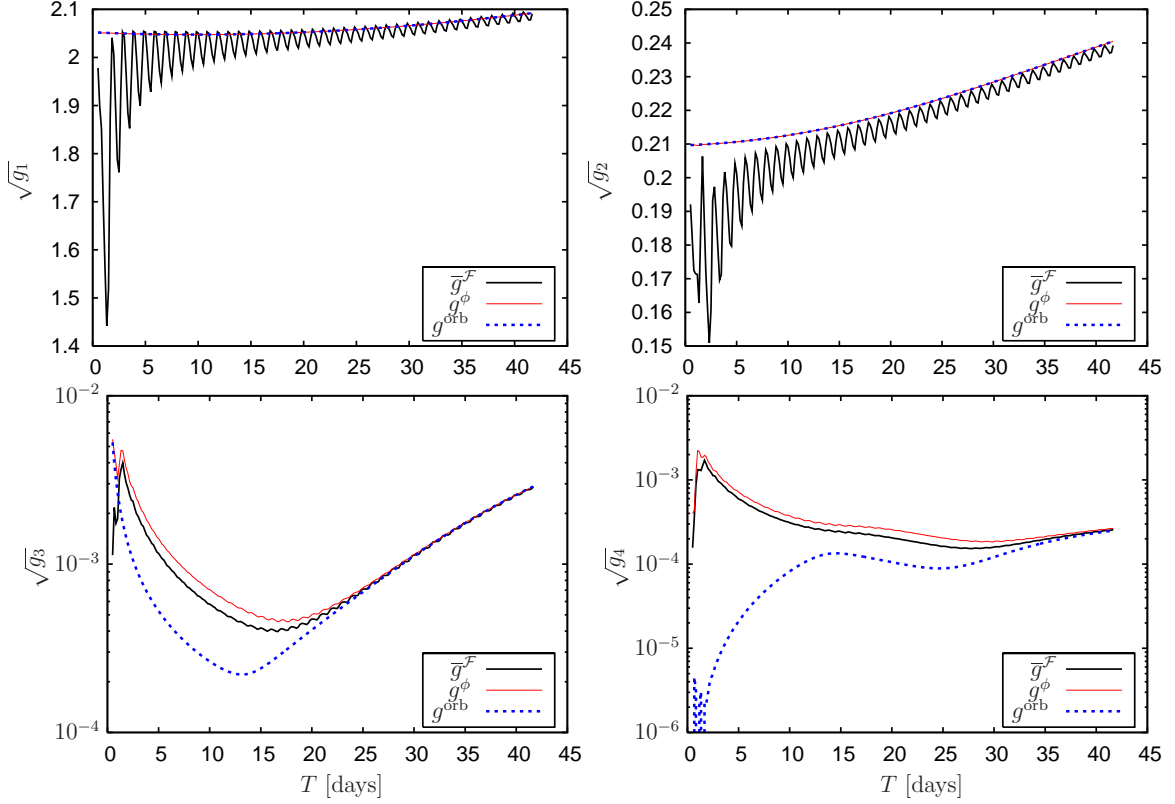


FIG. 8: Square roots of the four eigenvalues g_i of different metric approximations (in natural units) as functions of observation time T . [Same parameters as in Fig. 7]

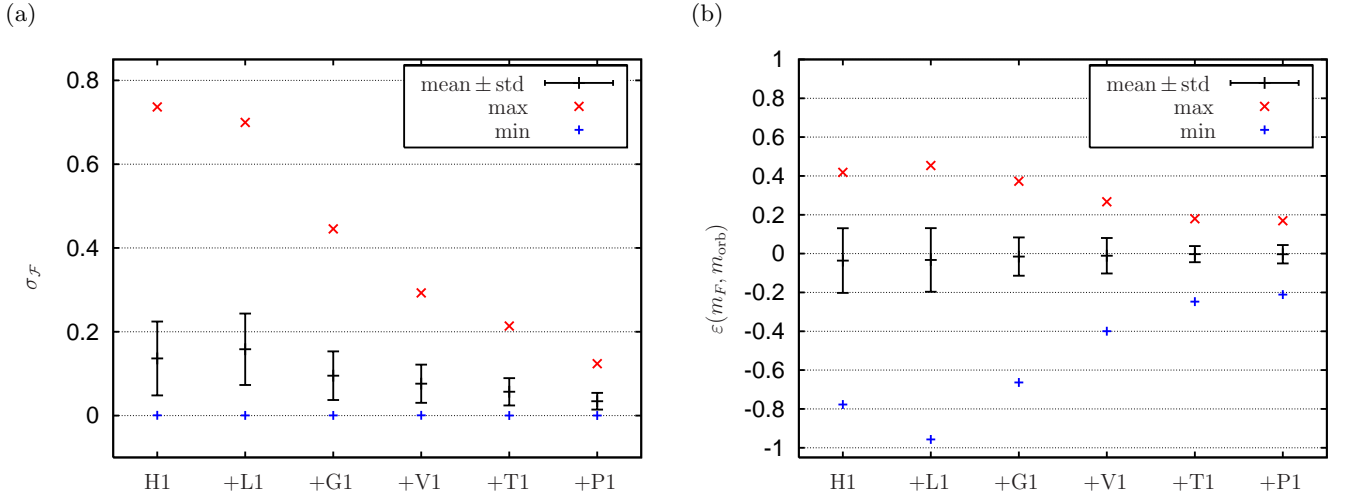


FIG. 9: Distribution of (a) intrinsic relative \mathcal{F} -metric uncertainty $\sigma_{\mathcal{F}}$ and (b) relative errors $\varepsilon(m_{\mathcal{F}}, m_{\text{orb}})$ as functions of the coherent combination of (assumed *equal-noise*) detectors, for $T = 55$ hours. Plotted are the mean, standard deviation and extremal values of the distribution for each detector combination. The assumed detectors (location and orientation only) are: 'H1' = LIGO Hanford, 'L1' = LIGO Livingston, 'G1' = GEO600, 'V1' = Virgo, 'T1' = TAMA, 'P1' = Caltech 40m.

Another effect seen in these figures is a systematic deviation of m_0 with respect to $m_{\mathcal{F}}$ with increasing mismatches, which becomes noticeable at around $m_{\mathcal{F}} \gtrsim 0.15$. This deviation would be suspected due to higher-

order corrections $\mathcal{O}(\Delta\lambda^3)$ with respect to the local metric expansion, and is found to be roughly independent of the observation time T . We can approximate this systematic deviation by an empirical quadratic correction of

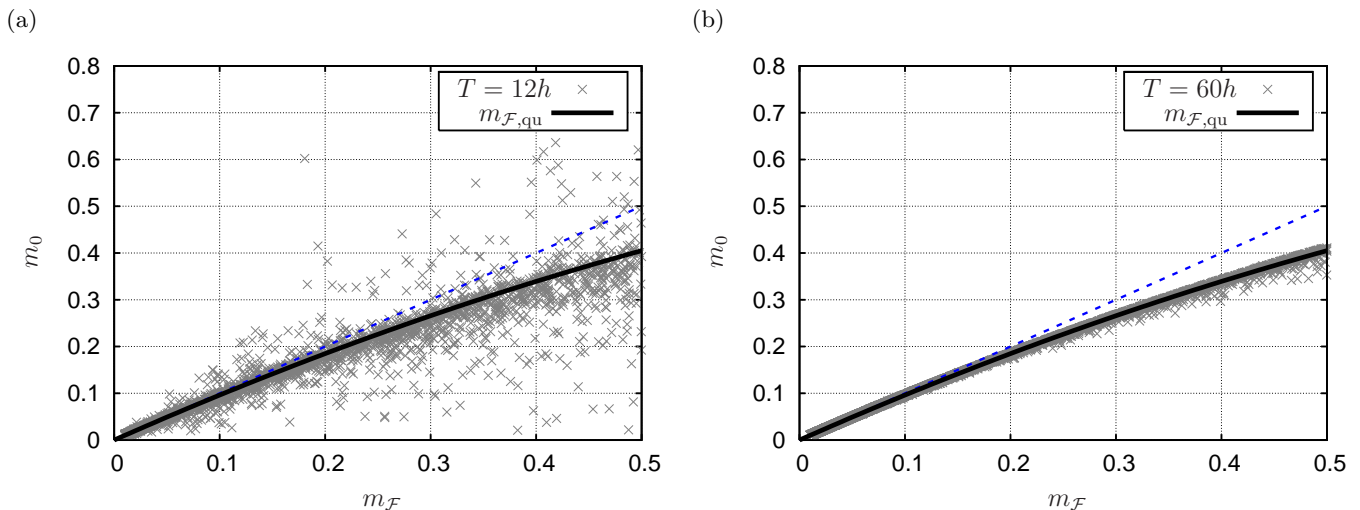


FIG. 10: Measured mismatches m_0 versus predicted \mathcal{F} -mismatches $m_{\mathcal{F}}$ for observations times of (a) $T = 12$ hours and (b) $T = 60$ hours, omitting points with $\Delta\hat{\Omega} > 5$. The dashed line indicates the identity function.

the form

$$m_{\mathcal{F},\text{qu}}(m_{\mathcal{F}}) = m_{\mathcal{F}} - 0.38 m_{\mathcal{F}}^2, \quad (124)$$

which can be used in comparisons to measured mismatches, as it compensates for the systematic “drift” in m_0 . Note that this deviation makes the metric a conservative over-estimate, as the actual mismatches tend to be smaller than the predicted ones.

1. Metric problems for $T \lesssim 1$ day

The strong scattering of mismatches seen in Fig. 10(a) for short observation times can be attributed to an intrinsic property of the \mathcal{F} -statistic: namely, the “local” parameter-space structure for short observation times is not very well approximated by a quadratic form in offsets. Note that obviously the metric approximation is valid in the strict *local* sense of sufficiently small offsets, but in practice we are more interested in a finite “local” region of small mismatches, $m \lesssim 0.5$ say. An illustrative example for this is shown in Figs. 11, 12, where we have measured the \mathcal{F} -statistic (using `lalapps_ComputeFStatistic`) over a $\sim 10^{-4}$ Hz band around the true signal frequency, with the other Doppler parameters (α, δ, \dot{f}) held fixed at their correct values. For an observation time of $T = 5$ hours, the quadratic decrease predicted by the \mathcal{F} -metric is clearly not a good approximation, as can be seen in Fig. 11: depending on the sign of the frequency offset, the metric would either substantially under- or overestimate the mismatch. This effect decreases rapidly with observation time, and for $T = 30$ hours (and the same signal), the decrease of the \mathcal{F} -statistic is “locally” much better approximated by the metric, as seen in Fig. 12. This effect can be understood as follows: the quadratic decrease of the \mathcal{F} -statistic predicted by the metric has a typical width in

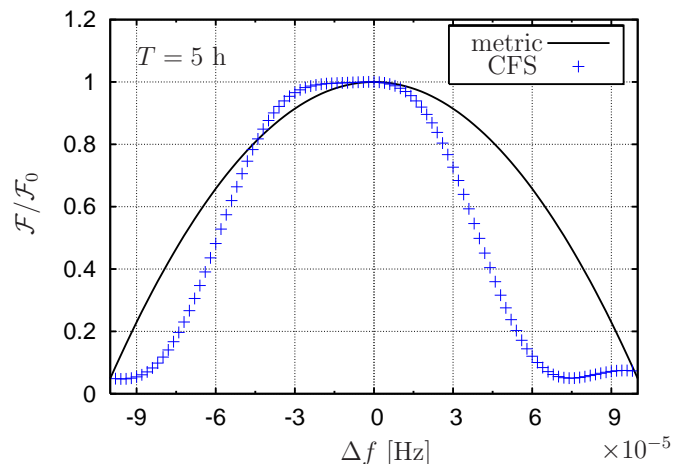


FIG. 11: Comparison of the measured decrease in \mathcal{F} -statistic (CFS) as a function of frequency offset Δf , and the corresponding metric prediction $1 - m_{\mathcal{F}}$, for an observation time of $T = 5$ hours. [Parameters: $f = 100$ Hz, $\cos \iota = 0.95$, $\psi = 2.25$, $\alpha = 5.98$, $\delta = 0.09$, $\dot{f} = 0$]

frequency of $\Delta f_0 \sim 1/T$ (cf. Sect. IV B). However, the spin motion of the earth creates “side-lobes” in frequency space at offsets of a few $f_{\text{spin}} = 1/\text{day} \sim 10^{-5}$ Hz, which are clearly visible in Fig. 12. For observation times much smaller than a day, these side-lobes are therefore not well separated from the main peak and will substantially alter its quadratic form, e.g. by creating “plateaus” and steeper “cliffs”, as seen in Fig. 11. As the observation time gets longer, i.e. $T \gtrsim 1$ day, the main peak becomes well separated, and therefore well described by the metric approximation.

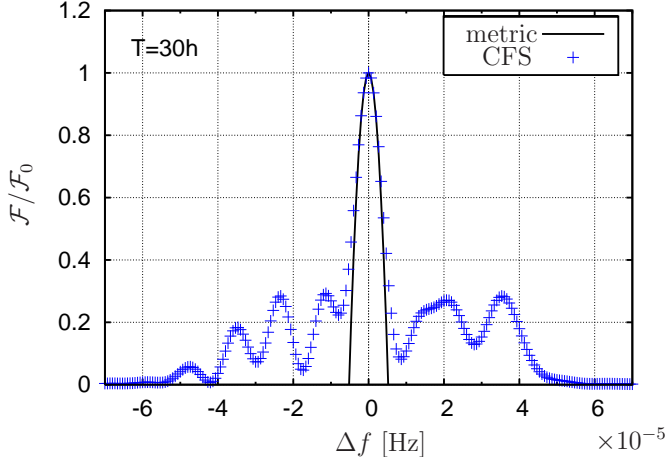


FIG. 12: Same as Fig. 11 for an observation time of $T = 30$ hours.

2. Metric problems for $\Delta\hat{\Omega} > 5$

As already mentioned, another problem with the metric approximation affects points with large angular offsets $\Delta\hat{\Omega}$, and is present even for long observation times. This can be seen in Fig. 13, showing the relative errors $\varepsilon(m_0, m_{\mathcal{F}, \text{qu}})$ as a function of angular offset $\Delta\hat{\Omega}$, for observation times $T > 48$ hours. For angular offsets $\Delta\hat{\Omega} <$

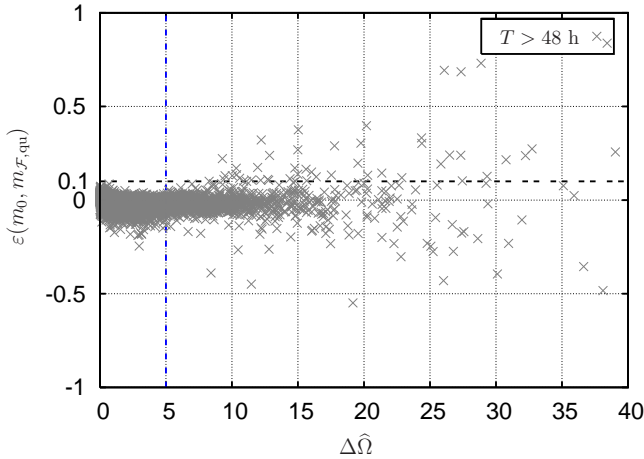


FIG. 13: Relative errors $\varepsilon(m_0, m_{\mathcal{F}, \text{qu}})$ versus angular offset $\Delta\hat{\Omega}$ in natural units, for observation times $T > 48$ hours. For better readability of the figure, the displayed range of angular offsets is limited to $\Delta\hat{\Omega} \leq 40$.

5, the relative errors stay below $\varepsilon(m_0, m_{\mathcal{F}, \text{qu}}) < 0.1$, but with increasing $\Delta\hat{\Omega}$, the errors start to spread out substantially.

The reason for this metric failure can be traced to the curvature of the metric on the sky. While the metric ellipses have constant orientation as functions of frequency and spindown, their orientation changes with sky posi-

tion. This curvature is closely related to the global “circles in the sky” (CiS) structure discussed in [5], as the metric ellipses on the sky are “tangential” to these circles. To first order, the CiS are described by the equation

$$f \left(1 + \vec{n} \cdot \vec{V}/c \right) = f_s \left(1 + \vec{n}_s \cdot \vec{V}/c \right), \quad (125)$$

where f and \vec{n} are the “target” frequency and sky position respectively, while f_s and \vec{n}_s are the corresponding signal parameters. The problem stems from the curva-

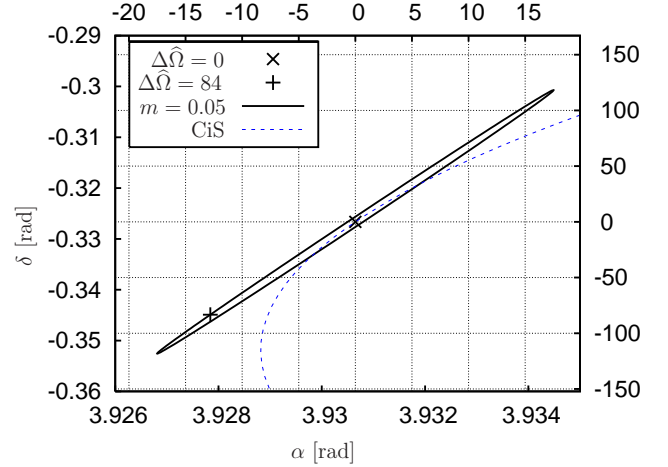


FIG. 14: Metric “failure” for large angular offset $\Delta\hat{\Omega} = 84$ at $T = 68$ hours. The point ‘x’ indicates the signal location, ‘+’ shows an offset location on the $m = 0.05$ iso-mismatch ellipse with a measured mismatch of $m_0 \sim 1$. The dashed line indicates the “circle in the sky” (125) defined by the signal location. The top and right-hand axes show the offsets in natural units. [Parameters: $f = 186.34$ Hz, $\alpha = 3.93$, $\delta = -0.33$, $\dot{f} = 1.7 \times 10^{-10} \text{ s}^{-2}$, $\cos \iota = 0.4$, $\psi = 1.65$]

ture of the \mathcal{F} -statistic circles in the sky-coordinates α , δ , which is why the CiS is only locally well approximated by the respective mismatch ellipses. This effect is seen clearly in Fig. 14, which shows an extreme example of such a metric “failure” due to large $\Delta\hat{\Omega}$. In this figure, ‘+’ indicates a sky position on the $m_{\mathcal{F}} = 0.05$ iso-mismatch ellipse, which has an angular offset from the signal of $\Delta\hat{\Omega} = 84$. Contrary to the predicted mismatch, the measured mismatch at this point is $m_0 \sim 1$, as the \mathcal{F} -statistic decreases rapidly away from the CiS (indicated by the dashed line).

3. Summary of metric validation

Fig. 15 summarizes the relative errors $\varepsilon(m_0, m_{\mathcal{F}, \text{qu}})$ between the (quadratically corrected) predictions (124) and the measured mismatches m_0 , as a function of observation time T . We see that, as expected, excluding large angular offsets ($\Delta\hat{\Omega} > 5$) yields a substantially improved

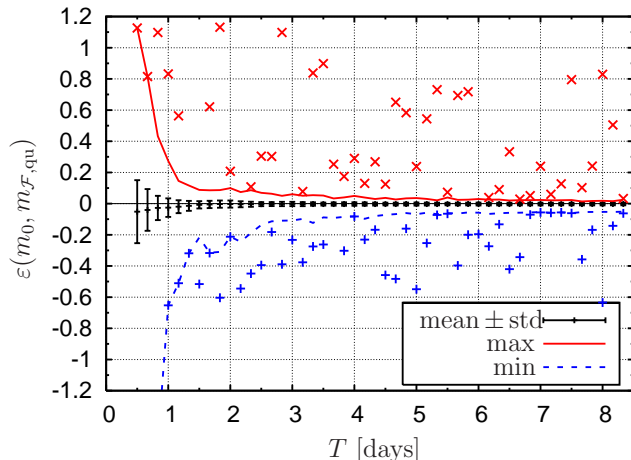


FIG. 15: Distribution of relative errors $\varepsilon(m_0, m_{\mathcal{F}, \text{qu}})$ as a function of observation time T . Plotted are the mean, standard deviation and extremal values of the distribution for each value of T , excluding points with $\Delta\hat{\Omega} > 5$. The points 'x' and '+' indicate the respective maximum and minimum errors when including results with $\Delta\hat{\Omega} > 5$.

agreement between the metric prediction and the measurements, as it eliminates the type of “metric failures” discussed in IV G 2. We also see that the relative errors can still be quite large for short observation times $T \lesssim 1$ day, as discussed in IV G 1, and that these errors decrease rapidly with T . For observation times of $T \gtrsim 1$ day, the average error is below a few percent. We can therefore conclude that the agreement of the \mathcal{F} -metric with the measurements is very good in the domain of applicability of the metric approximation.

V. DISCUSSION

We have derived a formalism for the general parameter-space metric of the multi-detector \mathcal{F} -statistic, and we have explicitly computed the metric for signals from isolated spinning neutron stars. We have shown that there exists a family of \mathcal{F} -metrics, parametrized by the two (unknown) amplitude parameters ψ and $\cos\iota$. We explicitly derived the extremal “mismatch bounds” (i.e. the maximum and minimum possible mismatches) of the \mathcal{F} -metric family, and we introduced an average \mathcal{F} -metric, which is independent of the unknown amplitude parameters. We have shown that the multi-detector \mathcal{F} -metric does not scale with the number of detectors. Combining detectors coherently therefore does not increase the required number of templates. In the long-duration limit ($T \gtrsim 1$ month), we found that the \mathcal{F} -metric family converges towards a simple orbital metric g_{ij}^{orb} , which neglects both the amplitude modulation and the phase modulation caused by the diurnal rotation of the Earth.

Both the orbital and the closely related phase metric provide relatively good mismatch approximations in

practice, and the quality of these approximations improves with longer observation times and with the number of coherently-combined detectors.

The orbital metric, however, while virtually identical to the phase metric for almost all directions in parameter space, was found to be substantially more degenerate for observation times shorter than a month. This has important consequences for the covering problem of the parameter space and requires further study. Finally, we have identified two regimes in which the local metric approximation itself is not very reliable: namely, for observation times $T \lesssim 1$ day, and for large angular offsets $\Delta\hat{\Omega} \gtrsim 5$ (in natural units).

APPENDIX A: ALTERNATIVE DERIVATION OF THE \mathcal{F} -METRIC

A more elegant derivation of the \mathcal{F} -metric (47) can be obtained [20] by projecting the full parameter-space metric in $\{\mathcal{A}, \lambda\}$ into the reduced parameter space λ of the \mathcal{F} -statistic. We denote the full parameter space as $\theta = \{\mathcal{A}, \lambda\}$, and we use index conventions $\theta^a = \{\mathcal{A}^\mu, \lambda^i\}$. Recall the form of the log-likelihood ratio (15), namely

$$\ln \Lambda(\mathbf{x}; \theta) \equiv (\mathbf{x}|\mathbf{s}(\theta)) - \frac{1}{2} (\mathbf{s}(\theta)|\mathbf{s}(\theta)). \quad (\text{A1})$$

If the data contains a signal with parameters θ_s , i.e. $\mathbf{x}(t) = \mathbf{n}(t) + \mathbf{s}(t; \theta_s)$, and if the target position θ is “close” to the signal location, i.e. $\theta = \theta_s + \Delta\theta$ for “small” $\Delta\theta$, then the expectation value of $\ln \Lambda$ can be expanded as

$$2E[\ln \Lambda(\theta|\theta_s)] = (\mathbf{s}|\mathbf{s}) - (\partial_a \mathbf{s}|\partial_b \mathbf{s}) \Delta\theta^a \Delta\theta^b + \mathcal{O}(3), \quad (\text{A2})$$

so the full parameter-space metric \tilde{g}_{ab} is found as

$$\tilde{g}_{ab} = \frac{(\partial_a \mathbf{s}|\partial_b \mathbf{s})}{(\mathbf{s}|\mathbf{s})}. \quad (\text{A3})$$

This expression is sometimes referred to as the *normalized* Fisher matrix [4]. As mentioned in the introduction, this “canonical” metric differs from a definition often found in the literature (e.g. [1, 2, 12]), which is based on a somewhat more *ad-hoc* measure of the “match”, namely $M \equiv (\mathbf{s}(\theta_s)|\mathbf{s}(\theta))$, instead of the full log-likelihood (A1). As it turns out, both definitions result in the same phase metric (107) when considering constant-amplitude signals (after minimizing the mismatch (A3) over the unknown amplitude). In general, however, the canonical definition (A3), and correspondingly (46), is more directly relevant to the covering problem, as it describes the relative loss of detection statistic. For the assumed general form of the signal (1), we have

$$\rho^2(0) \equiv (\mathbf{s}|\mathbf{s}) = \mathcal{A}^\mu \mathcal{M}_{\mu\nu} \mathcal{A}^\nu, \quad (\text{A4})$$

and the respective derivatives with respect to the amplitude and Doppler subspaces are given by

$$\partial_\mu \mathbf{s} = \frac{\partial \mathbf{s}}{\partial A^\mu} = \mathbf{h}_\mu(t; \lambda), \quad (\text{A5})$$

$$\partial_i \mathbf{s} = \frac{\partial \mathbf{s}}{\partial \lambda^i} = \mathcal{A}^\mu \partial_i \mathbf{h}_\mu. \quad (\text{A6})$$

The full metric \tilde{g}_{ab} therefore consists of the three blocks (with respect to the two subspaces):

$$\tilde{g}_{ab} = \rho^{-2}(0) \begin{pmatrix} \mathcal{M}_{\mu\nu} & \mathcal{A}^\nu \mathcal{R}_{\mu\nu i} \\ \mathcal{A}^\nu \mathcal{R}_{\mu\nu i} & \mathcal{A}^\alpha h_{\alpha\beta ij} \mathcal{A}^\beta \end{pmatrix}, \quad (\text{A7})$$

in terms of h_{ij} and \mathcal{R}_i defined in (40) and (31). The \mathcal{F} -metric $g_{ij}^{\mathcal{F}}$ in the Doppler subspace can be regarded as the distance corresponding to given Doppler offsets $\Delta\theta^i = \Delta\lambda^i$, *minimized* over the amplitude offsets $\Delta\theta^\mu = \Delta\mathcal{A}^\mu$, i.e.

$$g_{ij}^{\mathcal{F}} \Delta\lambda^i \Delta\lambda^j \equiv \min_{\Delta\mathcal{A}^\mu} \tilde{g}_{ab} \Delta\theta^a \Delta\theta^b. \quad (\text{A8})$$

This can be minimized trivially, since it is a quadratic function in $\Delta\mathcal{A}^\mu$, and the ‘‘compensating’’ amplitude mismatches are

$$\Delta\theta^\mu = -\hat{g}^{\mu\nu} \tilde{g}_{\nu i} \Delta\theta^i, \quad (\text{A9})$$

where $\hat{g}^{\mu\nu}$ is the inverse matrix of $\tilde{g}_{\mu\nu}$, i.e. $\hat{g}^{\mu\alpha} \tilde{g}_{\alpha\nu} = \delta_\nu^\mu$. Inserting this into (A8) we obtain

$$g_{ij}^{\mathcal{F}} = \tilde{g}_{ij} - \tilde{g}_{i\mu} \hat{g}^{\mu\nu} \tilde{g}_{\nu j}, \quad (\text{A10})$$

which corresponds to the *projection* of the full metric \tilde{g}_{ab} into the Doppler subspace. Using the explicit components (A7), we find

$$g_{ij}^{\mathcal{F}}(\mathcal{A}) = \rho^{-2}(0) \mathcal{A} [h_{ij} - \mathcal{R}_i^T \mathcal{M}^{-1} \mathcal{R}_j] \mathcal{A} \quad (\text{A11})$$

$$= \frac{\mathcal{A} \cdot \mathcal{G}_{ij} \cdot \mathcal{A}}{\mathcal{A} \cdot \mathcal{M} \cdot \mathcal{A}}, \quad (\text{A12})$$

in perfect agreement with the earlier result (48), which was obtained in a more straightforward, but somewhat more tedious calculation.

APPENDIX B: \mathcal{F} -METRIC FOR LOW-FREQUENCY SIGNALS

In the case of low frequencies f_s (which would be relevant for LISA) and/or short observation times T , where $f_s T \gg 10^4$, we cannot use the simplifying approximation of Sect. III D. We can nevertheless proceed in the same way: using the expansion (64) and keeping only leading-order terms, we can express (40) as

$$h_{\mu\nu ij} \approx \frac{1}{2} \mathcal{S}^{-1} T \begin{pmatrix} P_{ij}^1 & P_{ij}^3 & 0 & P_{ij}^4 \\ P_{ij}^3 & P_{ij}^2 & -P_{ij}^4 & 0 \\ 0 & -P_{ij}^4 & P_{ij}^1 & P_{ij}^3 \\ P_{ij}^4 & 0 & P_{ij}^3 & P_{ij}^2 \end{pmatrix}, \quad (\text{B1})$$

in terms of the four independent components

$$\begin{aligned} P_{ij}^1 &= \langle \partial_i a \partial_j a \rangle_S + \langle a^2 \partial_i \phi \partial_j \phi \rangle_S, \\ P_{ij}^2 &= \langle \partial_i b \partial_j b \rangle_S + \langle b^2 \partial_i \phi \partial_j \phi \rangle_S, \\ P_{ij}^3 &= \langle \partial_i a \partial_j b \rangle_S + \langle a b \partial_i \phi \partial_j \phi \rangle_S, \\ P_{ij}^4 &= \langle b \partial_i a \partial_j \phi \rangle_S - \langle a \partial_i b \partial_j \phi \rangle_S, \end{aligned} \quad (\text{B2})$$

with implicit symmetrization in i, j . In a similar manner we calculate $\mathcal{R}_{\mu\nu i}$, defined in (31), which yields

$$\mathcal{R}_{\mu\nu i} \approx \frac{1}{2} \mathcal{S}^{-1} T \begin{pmatrix} \hat{\mathcal{R}}_i & \tilde{\mathcal{R}}_i \\ -\tilde{\mathcal{R}}_i & \hat{\mathcal{R}}_i \end{pmatrix}, \quad (\text{B3})$$

where the 2x2 matrices $\hat{\mathcal{R}}_i$ and $\tilde{\mathcal{R}}_i$ are defined as

$$\hat{\mathcal{R}}_i \equiv \begin{pmatrix} R_i^{11} & R_i^{12} \\ R_i^{21} & R_i^{22} \end{pmatrix}, \text{ and } \tilde{\mathcal{R}}_i \equiv \begin{pmatrix} R_i^{13} & R_i^{14} \\ R_i^{14} & R_i^{24} \end{pmatrix}, \quad (\text{B4})$$

in terms of

$$\begin{aligned} R_i^{11} &= \langle a \partial_i a \rangle_S, & R_i^{12} &= \langle a \partial_i b \rangle_S, \\ R_i^{21} &= \langle b \partial_i a \rangle_S, & R_i^{22} &= \langle b \partial_i b \rangle_S, \\ R_i^{13} &= \langle a^2 \partial_i \phi \rangle_S, & R_i^{24} &= \langle b^2 \partial_i \phi \rangle_S, \\ R_i^{14} &= \langle a b \partial_i \phi \rangle_S. \end{aligned} \quad (\text{B5})$$

Note that $\hat{\mathcal{R}}_i$ only contains derivatives of the antenna-pattern functions a^X, b^X (which were neglected in Sect. III D), while $\tilde{\mathcal{R}}_i$ only contains derivatives of the phase. As a consequence of this block structure, one finds

$$\{\text{T} \mathcal{R}_i \mathcal{M}^{-1} \mathcal{R}_j\}_{\mu\nu} \approx \frac{1}{2} \mathcal{S}^{-1} T \begin{pmatrix} Q_{ij}^1 & Q_{ij}^3 & 0 & Q_{ij}^4 \\ Q_{ij}^3 & Q_{ij}^2 & -Q_{ij}^4 & 0 \\ 0 & -Q_{ij}^4 & Q_{ij}^1 & Q_{ij}^3 \\ Q_{ij}^4 & 0 & Q_{ij}^3 & Q_{ij}^2 \end{pmatrix}, \quad (\text{B6})$$

with the four independent components

$$\begin{aligned} D Q_{ij}^1 &= A [R_i^{21} R_j^{21} + R_i^{14} R_j^{14}] + B [R_i^{11} R_j^{11} + R_i^{13} R_j^{13}] \\ &\quad - 2C [R_i^{11} R_j^{21} + R_i^{13} R_j^{14}], \\ D Q_{ij}^2 &= A [R_i^{24} R_j^{24} + R_i^{22} R_j^{22}] + B [R_i^{14} R_j^{14} + R_i^{12} R_j^{12}] \\ &\quad - 2C [R_i^{14} R_j^{24} + R_i^{12} R_j^{22}], \\ D Q_{ij}^3 &= A [R_i^{14} R_j^{24} + R_i^{22} R_j^{21}] + B [R_i^{14} R_j^{13} + R_i^{12} R_j^{11}] \\ &\quad - C [R_i^{24} R_j^{13} + R_i^{14} R_j^{14} + R_i^{11} R_j^{22} + R_i^{12} R_j^{21}], \\ D Q_{ij}^4 &= A [R_i^{21} R_j^{24} - R_i^{14} R_j^{22}] + B [R_i^{11} R_j^{14} - R_i^{12} R_j^{13}] \\ &\quad - C [R_i^{11} R_j^{24} - R_i^{13} R_j^{22} + R_i^{14} R_j^{21} - R_i^{12} R_j^{14}]. \end{aligned} \quad (\text{B7})$$

Putting all the pieces together, we find \mathcal{G}_{ij} , defined in (44), in the form:

$$\mathcal{G}_{\mu\nu} \approx \frac{1}{2} \mathcal{S}^{-1} T \begin{pmatrix} m^1 & m^3 & 0 & m^4 \\ m^3 & m^2 & -m^4 & 0 \\ 0 & -m^4 & m^1 & m^3 \\ m^4 & 0 & m^3 & m^2 \end{pmatrix}, \quad (\text{B8})$$

in terms of the *four* components ($r = 1, 2, 3, 4$):

$$m^r \equiv (P_{ij}^r - Q_{ij}^r) \Delta\lambda^i \Delta\lambda^j. \quad (\text{B9})$$

As discussed in Sect. III, the extrema $\widehat{m}_{\mathcal{F}}$ are the eigenvalues of $\mathcal{M}^{-1} \cdot \mathcal{G}$, which are the solutions of

$$0 = \det \mathcal{M}^{-1} \det [\mathcal{G} - \widehat{m}_{\mathcal{F}} \mathcal{M}] , \quad (\text{B10})$$

or equivalently

$$0 = (m^1 - \widehat{m}_{\mathcal{F}} A)(m^2 - \widehat{m}_{\mathcal{F}} B) - (m^3 - \widehat{m}_{\mathcal{F}} C)^2 - (m^4)^2 . \quad (\text{B11})$$

We see that there are again maximally *two* independent eigenvalues, namely

$$\widehat{m}_{\mathcal{F}}^{\max|\min}(\lambda; \Delta\lambda) = \overline{m}_{\mathcal{F}} \pm \sqrt{\overline{m}_{\mathcal{F}}^2 - \widetilde{m}^2} , \quad (\text{B12})$$

with

$$\begin{aligned} \overline{m}_{\mathcal{F}} &= (2D)^{-1} [Bm^1 + Am^2 - 2Cm^3] , \\ \widetilde{m} &= D^{-1} [m^1 m^2 - (m^3)^2 - (m^4)^2] , \end{aligned} \quad (\text{B13})$$

which is formally very similar to the earlier result (90).

ACKNOWLEDGMENTS

I am very grateful to Curt Cutler for numerous helpful suggestions, and I thank Chris Messenger, Andrzej Królak, Badri Krishnan and Ben Owen for useful discussions and comments.

-
- [1] R. Balasubramanian, B. S. Sathyaprakash, and S. V. Dhurandhar, *Phys. Rev. D.* **53**, 3033 (1996).
 - [2] B. J. Owen, *Phys. Rev. D.* **53**, 6749 (1996).
 - [3] T. A. Apostolatos, *Phys. Rev. D.* **52**, 605 (1995).
 - [4] A. Królak, M. Tinto, and M. Vallisneri, *Phys. Rev. D.* **70**, 022003 (2004).
 - [5] R. Prix and Y. Itoh, *Class. Quant. Grav.* **22**, S1003 (2005).
 - [6] R. Prix et al. (LIGO Scientific Collaboration), submitted (2006).
 - [7] P. Jaranowski, A. Królak, and B. F. Schutz, *Phys. Rev. D.* **58**, 063001 (1998).
 - [8] B. Abbott et al. (LIGO Scientific Collaboration), *Phys. Rev. D.* **69**, 082004 (2004).
 - [9] B. Abbott et al. (LIGO Scientific Collaboration), submitted (2006), gr-qc/0605028.
 - [10] P. Astone et al., *Class. Quant. Grav.* **22**, 1243 (2005).
 - [11] C. Cutler and B. F. Schutz, *Phys. Rev. D.* **72**, 063006 (2005).
 - [12] N. J. Cornish and E. K. Porter, *Class. Quant. Grav.* **22**, S927 (2005).
 - [13] P. R. Brady, T. Creighton, C. Cutler, and B. F. Schutz, *Phys. Rev. D.* **57**, 2101 (1998).
 - [14] D. I. Jones, B. J. Owen, and D. Whitbeck, in preparation (2006).
 - [15] LIGO Scientific Collaboration, *LAL/LALApps: FreeSoftware (GPL) tools for data-analysis.*, <http://www.lsc-group.phys.uwm.edu/daswg/>.
 - [16] L. S. Finn, *Phys. Rev. D.* **46**, 5236 (1992).
 - [17] P. Jaranowski and A. Królak, *Living Reviews in Relativity* **8**, 3 (2005).
 - [18] Y. Pan, A. Buonanno, Y. Chen, and M. Vallisneri, *Phys. Rev. D.* **69**, 104017 (2004).
 - [19] A. Buonanno, Y. Chen, Y. Pan, H. Tagoshi, and M. Vallisneri, *Phys. Rev. D.* **72**, 084027 (2005).
 - [20] C. Cutler, *private communication*.